Supplemental material to this article can be found at:
http://molpharm.aspetjournals.org/content/suppl/2020/08/12/molpharm.120.000054.DC1
1521-0111/98/4/364–381$35.00
MOLECULAR PHARMACOLOGY
https://doi.org/10.1124/molpharm.120.000054
Mol Pharmacol 98:364–381, October 2020

Pharmacology and Molecular Mechanisms of Clinically Relevant Estrogen Estetrol and Estrogen Mimic BMI-135 for the Treatment of Endocrine-Resistant Breast Cancer[S]

Balkees Abderrahman, Philipp Y. Maximov, Ramona F. Curpan, Jay S. Hanspal, Ping Fan, Rui Xiong, Debra A. Tonetti, Gregory R.J. Thatcher, and V. Craig Jordan

Department of Breast Medical Oncology, University of Texas MD Anderson Cancer Center, Houston, Texas (B.A., P.Y.M., J.S.H., P.F., V.C.J.); Coriolan Dragulescu Institute of Chemistry, Romanian Academy, Timisoara, Romania (R.F.C.); and Department of Pharmaceutical Sciences, University of Illinois at Chicago, Chicago, Illinois (R.X., D.A.T., G.R.J.T.)

Received May 2, 2020; accepted July 28, 2020

ABSTRACT

Long-term estrogen deprivation (LTED) with tamoxifen (TAM) or aromatase inhibitors leads to endocrine-resistance, whereby physiologic levels of estrogen kill breast cancer (BC). Estrogen therapy is effective in treating patients with advanced BC after resistance to TAM and aromatase inhibitors develops. This therapeutic effect is attributed to estrogen-induced apoptosis via the estrogen receptor (ER). Estrogen therapy can have unpleasant gynecologic and nongynecologic adverse events. Here, we study estetrol (E_4) and a model Selective Human ER Partial Agonist (ShERPA) BMI-135. Estetrol and ShERPA TTC-352 are being evaluated in clinical trials. These agents are proposed as safer estrogenic candidates compared with 17β-estradiol (E_2) for the treatment of endocrine-resistant BC. Cell viability assays, real-time polymerase chain reaction, luciferase reporter assays, chromatin immunoprecipitation, docking and molecular dynamics simulations, human unfolded protein response (UPR) RT^2 PCR profiler arrays, live cell microscopic imaging and analysis, and annexin V staining assays were conducted. Our work was done in eight biologically different human BC cell lines and one human endometrial cancer cell line, and results were compared with full agonists estrone, E_2, and estriol, a benchmark partial agonist triphenylethylene bisphenol (BPTPE), and antagonists 4-hydroxytamoxifen and endoxifen. Our study shows the pharmacology of E_4 and BMI-135 as less-potent full-estrogen agonists as well as their molecular mechanisms of tumor regression in LTED BC through triggering a rapid UPR and apoptosis. Our work concludes that the use of a full agonist to treat BC is potentially superior to a partial agonist given BPTPE's delayed induction of UPR and apoptosis, with a higher probability of tumor clonal evolution and resistance.

SIGNIFICANCE STATEMENT

Given the unpleasant gynecologic and nongynecologic adverse effects of estrogen treatment, the development of safer estrogens for endocrine-resistant breast cancer (BC) treatment and hormone replacement therapy remains a priority. The naturally occurring estrogen estetrol and Selective Human Estrogen-Receptor Partial Agonists are being evaluated in endocrine-resistant BC clinical trials. This work provides a comprehensive evaluation of their pharmacology in numerous endocrine-resistant BC models and an endometrial cancer model and their molecular mechanisms of tumor regression through the unfolded protein response and apoptosis.

Introduction

In 1944, Sir Alexander Haddow used high-dose synthetic estrogen therapy to treat metastatic breast cancer (MBC) (Haddow et al., 1944) in patients who were long-term (≥5 years past menopause) estrogen-deprived (LTED) (Haddow, 1970). A 30% response rate was reported. High-dose estrogen therapy was used for 30 years prior to the introduction of tamoxifen (TAM) (Jordan, 2003). Tamoxifen was preferred because of the lower incidence of adverse events (AEs) (Cole et al., 1971; Ingle et al., 1981). In the 1970s, the translational research proposal of long-term adjuvant antihormone TAM therapy was successfully advanced (Jordan et al., 1979; Jordan and Allen, 1980). This strategy established TAM as the agent of choice for adjuvant therapy (Early Breast Cancer Trialists' Collaborative Group, 1998).

Acquired resistance to TAM therapy in vivo initially involves the growth of breast cancer (BC) populations within 1 to 2 years that are TAM- and estrogen-dependent (Gottardis and Jordan, 1988; Gottardis et al., 1989b). Subsequent studies in vivo demonstrated that 5 years of TAM treatment (mimicking the standard of care period at the time) leads to new BC populations that grow with TAM but die with physiologic levels of estrogen (Wolf and Jordan, 1993; Yao et al., 2000). This discovery explained (Jordan, 2008) why high-dose estrogen therapy was only effective ≥5 years past menopause in Haddow's original clinical studies (Haddow, 1970).

This work was supported by National Institutes of Health National Cancer Institute MD Anderson Cancer Center Support Grant [Grant CA016672] to Peter Pisters; the George and Barbara Bush Foundation for Innovative Cancer Research (V.C.J.); the Cancer Prevention Research Institute of Texas (CPRIT) for the Science and Technology Acquisition and Retention (STARs) and STARs Plus Awards (V.C.J.); the Dallas/Fort Worth Living Legend Fellowship of Cancer Research (B.A.); and the Coriolan Dragulescu Institute of Chemistry of the Romanian Academy [Project no. 1.1/2020] (R.F.C.).
Authors disclose no conflicts of interest.
https://doi.org/10.1124/molpharm.120.000054.
[S] This article has supplemental material available at molpharm.aspetjournals.org.

Physiologic estrogen in LTED BC cells triggers a cellular stress response named the unfolded protein response (UPR) and induces apoptosis (Song et al., 2001; Lewis et al., 2005a; Ariazi et al., 2011). Hosford et al. (2019) confirmed the involvement of the UPR and apoptosis in patient-derived estrogen-deprived estrogen receptor (ER)-positive xenografts treated with 17β-estradiol (E_2). This UPR and apoptosis–paired biology underpinning estrogen-induced tumor regression not only explains the earlier observational clinical science (Haddow, 1970) but also reaffirms estrogen's therapeutic potential for the treatment of endocrine-resistant BC.

Lønning et al. (2001) used high-dose estrogen therapy in postmenopausal women with advanced endocrine-resistant BC (median deprivation of 4 years). The conjugated equine estrogen arm in the Women's Health Initiative trial and its long-term follow-up (Anderson *et al.*, 2004; Chlebowski *et al.*, 2020; Jordan, 2020) unintentionally illustrated the clinical relevance of estrogen-induced tumor regression (Abderrahman and Jordan, 2016). The Women's Health Initiative trial had more than 75% of the postmenopausal women LTED for 10 years past menopause. When given estrogen replacement therapy, there were significant decreases in BC incidence and mortality (Anderson *et al.*, 2004; Roehm, 2015; Chlebowski *et al.*, 2020). Ellis et al. (2009) demonstrated the antitumor actions of low-dose estrogen therapy in postmenopausal women with advanced adjuvant aromatase inhibitor–resistant BC (deprivation $\geq$2 years). Iwase et al. (2013), using ethinylestradiol in patients with MBC (median age 63 years), had a 56% clinical benefit rate. Chalasani et al. (2014), using E_2 during 3-month exemestane breaks in patients with MBC, had measurable clinical activity. These clinical studies reaffirm the earlier laboratory findings that estrogen treatment after LTED with TAM in vivo leads to BC regression (Yao et al., 2000).

These in vivo and in vitro studies and clinical trials support the clinical benefit of using estrogen alone or in combination with growth inhibitors and/or apoptosis promoters for the treatment of endocrine-resistant BC. Nonetheless, concerns regarding AEs require the development of safer estrogens.

There are four naturally occurring forms of estrogen (Fig. 1): estrone (E_1), E_2, estriol (E_3), and estetrol (E_4).

Estetrol (Fig. 1), produced by the fetal liver during pregnancy (Holinka et al., 2008), is proposed as a promising estrogen for the treatment of advanced BC (Singer et al., 2014; Coelingh Bennink et al., 2017; Verhoeven et al., 2018; Schmidt et al., 2020), advanced prostate cancer (Dutman et al., 2017), use in hormone replacement therapy (Gérard et al., 2015; Coelingh Bennink et al., 2016; https://clinicaltrials.gov/ct2/show/NCT02834312), and in contraception (Creinin et al., 2019). In preclinical models, E_4 selectively activates the nuclear ERα, which plays a prominent role in the vasculoprotective action of estrogens (Abot et al., 2014). An ongoing phase I/IIA clinical trial of E_4 (Schmidt et al., 2020) shows the majority of patients experience favorable effects on wellbeing, and one patient completed both phases with stable disease after 24 weeks of treatment.

Selective Human ER Partial Agonists (ShERPAs), also known as selective estrogen mimics (Fig. 1), are novel benzothiophene [raloxifene (Ralox) or arzoxifene] derivatives with nanomolar potency designed to treat endocrine-resistant BC (Molloy et al., 2014; Xiong et al., 2016). The ShERPAs BMI-135 and TTC-352 were shown to cause tumor regression in TAM-resistant BC xenograft models and not to cause significant estrogen-like uterine growth in these models (Molloy et al., 2014; Xiong et al., 2016). An ongoing phase I clinical trial of TTC-352 (O'Regan et al., 2019) shows manageable safety and early clinical evidence of activity in patients with MBC progressing on endocrine therapy.

Given the clinical relevance of E_4 and ShERPAs, here we expand the study of their pharmacology in a broad range of BC and endometrial cancer cell lines and delineate their antitumor molecular mechanisms through triggering the UPR and apoptosis in select LTED and endocrine-resistant BC models.

Materials and Methods

Cell Culture and Reagents. E_1, E_2, E_3, E_4, and 4-hydroxyTAM (4OHT) were purchased from Sigma-Aldrich (St. Louis, MO). Endoxifen was purchased from Santa Cruz Biotechnology (Santa Cruz, CA), Ralox was purchased from Sigma-Aldrich, and ICI 182,780 fulvestrant (ICI) was purchased from Tocris Bioscience (Bristol, UK). Triphenylethylene bisphenol (BPTPE) was originally synthesized at the Organic Synthesis Facility, Fox Chase Cancer Center (Philadelphia, PA) (Maximov et al., 2010). The ShERPA BMI-135 was a gift from Dr. Debra Tonetti and Dr. Gregory R.J. Thatcher (University of Chicago, IL). The protein kinase regulated by RNA-like EnR kinase (PERK) inhibitor GSK G797800 was purchased from Toronto Research Chemicals (Toronto, ON, Canada). The inositol-requiring enzyme 1 (IRE1α) Inhibitor MKC-3946 was purchased from Calbiochem (San Diego, CA). Thioflavin T (ThT) was purchased from Sigma-Aldrich. All compounds except BMI-135 and E_4 were dissolved in ethanol, stored at −20°C, and protected from light. Compounds BMI-135 and E_4 were dissolved in DMSO. Wild-type (WT) estrogen-dependent BC cell line MCF-7:WS8 (Jiang et al., 1992); mutant p53 estrogen-dependent BC cell line T47D:A18 (Murphy et al., 1990b); the first in vitro cellular model recapitulating acquired-TAM resistance developed in athymic mice in vivo MCF-7:PF (Fan et al., 2014); estrogen-responsive, ER-positive, progesterone receptor–positive, and human epidermal growth factor receptor 2–positive luminal B BC cell line BT-474 (Kraus et al., 1987); estrogen-responsive, ER-positive, progesterone receptor–positive, and androgen receptor–positive luminal A BC cell line ZR-75-1 (Engel et al., 1978); antihormone-resistant estrogen-independent BC cell line MCF-7:5C (Lewis et al., 2005b); antihormone-sensitive estrogen-independent BC cell line MCF-7:2A (Pink et al., 1995); and antihormone (Ralox)-resistant estrogen-independent BC cell line MCF-7:RAL (Liu et al., 2003) were cultured

ABBREVIATIONS: AE, adverse event; ATF, activating transcription factor; BC, breast cancer; BPTPE, triphenylethylene bisphenol; ChIP, chromatin immunoprecipitation; CT, cycle threshold; DBPS, Dulbecco's phosphate-buffered saline; E_1, estrone; E_2, 17β-estradiol; E_3, estriol; E_4, estetrol; EnR, endoplasmic reticulum; ER, estrogen receptor; ERAD, EnR-associated degradation; ERE, estrogen-responsive element; FITC, fluorescein isothiocyanate; GREB1, Growth Regulation by Estrogen in Breast Cancer 1; ICI, ICI 182,780 fulvestrant; IRE1α, inositol-requiring enzyme 1; LBD, ligand-binding domain; LTED, long-term estrogen deprivation; MBC, metastatic BC; MBTPS1, Membrane Bound Transcription Factor Peptidase, Site 1; MD, molecular dynamics; 4OHT, 4-hydroxyTAM; PCR, polymerase chain reaction; PERK, protein kinase regulated by RNA-like EnR kinase; PI, propidium iodide; Ralox, raloxifene; RMSD, root-mean-square deviation; RMSF, root-mean-square fluctuation; RT-PCR, real-time PCR; SERM, Selective Estrogen Receptor Modulator; ShERPA, Selective Human Estrogen Receptor Partial Agonist; SRC-3, steroid receptor coactivator 3; TAM, tamoxifen; TFF1, trefoil factor 1; ThT, Thioflavin T; TPE, triphenylethylene; UPR, unfolded protein response; WT, wild type.

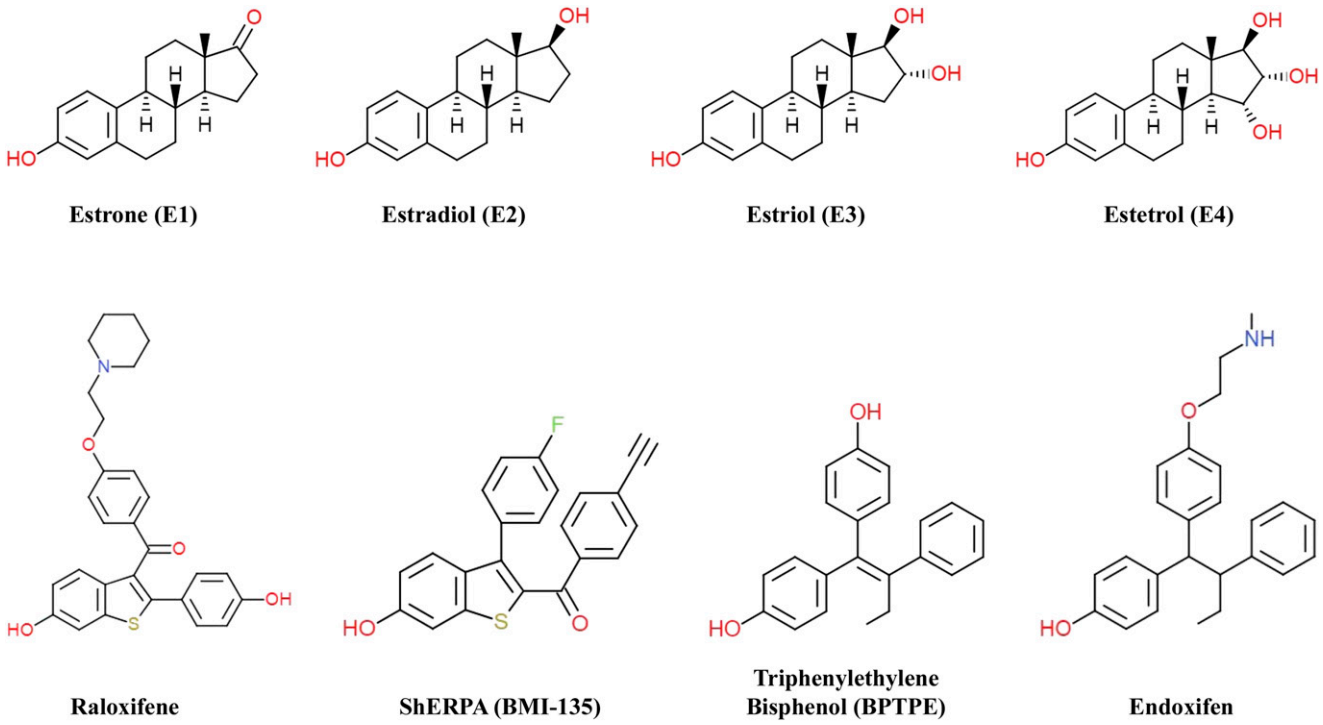

Fig. 1. Chemical structures of naturally occurring estrogens (E_1,E_2, E_3, and E_4), SERM raloxifene, synthesized ShERPA BMI-135 based on the benzothiophene scaffold of raloxifene, partial agonist BPTPE, and SERM endoxifen. The estrogen E_2 is the most potent estrogen. However, E_1 is generally 12 times less potent than E_2, and E_3 is generally 80 times less potent than E_2.

as previously described. Human endometrial adenocarcinoma cell line Ishikawa was cultured as previously described (Nishida et al., 1985). All cell cultures were done in T75 and T175 culture flasks (Thermo Fisher Scientific, Waltham, MA), passaged twice a week at 1:3 ratio, and grown in 5% CO_2 at 37°C. All cell lines were validated according to their short tandem repeat profiles at The University of Texas MD Anderson Cancer Center Characterized Cell Line Core. The short tandem repeat patterns of all cell lines were consistent with those from the Characterized Cell Line Core standard cells (Supplemental Table 1).

Cell Viability and Proliferation Assays. The biologic properties of test compounds (E_1, E_2, E_3, E_4, BMI-135, BPTPE, 4OHT, endoxifen, raloxifene, and ICI) in cells lines (MCF-7:WS8, T47D:A18, MCF-7:PF, BT-474, ZR-75-1, MCF-7:5C, MCF-7:2A, and MCF-7:RAL) were evaluated by assessing the DNA content of the cells as a measure of cell viability and proliferation using a DNA fluorescence Quantitation kit (Bio-Rad Laboratories, Hercules, CA) as previously described (Fan et al., 2013). The EC_{50} of all test compounds in different human BC and human endometrial cancer cell lines are summarized in Table 1. EC_{50} was calculated using the formula: Y = Bottom + (Top-Bottom)/(1 + 10^((LogEC$_{50}$-X)*HillSlope)).

Real-Time Polymerase Chain Reaction. MCF-7:WS8 and MCF-7:5C cells were seeded into six-well plates at a density of 100,000 cells/well. Cells were treated the next day with test compounds (E_2, BMI-135, BPTPE, and endoxifen) for 24 hours. RNA isolation, cDNA synthesis, and real-time polymerase chain reaction (RT-PCR) were performed as previously described (Obiorah et al., 2014). All primers were obtained from Integrated DNA Technologies Inc. (IDT, Coralville, IA) and validated by melt-curve analysis that revealed single peaks for all primer pairs. The primer sequences used for human trefoil factor 1 (TFF1) cDNA amplification were: 5′-CAT CGACGTCCCTCCAGAAGA-3′ sense, 5′-CTCTGGGACTAATCACCG TGCTG-3′ antisense; human Growth Regulation by Estrogen in Breast Cancer 1 (GREB1) gene: 5′-CAAAGAATAACCTGTTGGCCC-TGC-3′sense, 5′-GACATGCCTGCGCTCTCATACTTA-3′ antisense; and the reference gene 36B4: 5′-GTGTCCGACAATGGCAGCAT-3′ sense, 5′-GACACCCTCCAGGAAGCGA-3′ antisense.

TABLE 1

EC_{50} of test compounds in different human BC and human endometrial cancer cell lines

The EC_{50} was calculated to indicate potency differences between test compounds used in treating these cell lines over a specific period of time (Figs. 2 and 4), as indicated in the table.

Cell Line	Time Frame	Compound	E_1	E_2	E_3	E_4	BMI-135
MCF-7:5C	1 wk	EC_{50} (−log [M])	−9.19	−10.89	−10.04	−8.73	−8.39
MCF-7:5C	2 wk		−10.00	-	−10.31	−9.30	−8.98
MCF-7:2A	2 wk		−8.99	−10.74	−9.14	−8.50	−8.29
MCF-7:RAL	1 wk		−11.11	−12.99	−9.13	−10.07	−9.97
MCF-7:RAL	2 wk		−8.93	−11.06	−9.04	−7.22	−9.24
MCF-7:RAL	3 wk		−9.53	−10.89	−9.75	−8.38	−7.47
MCF-7:PF	1 wk		−8.68	−10.67	−9.43	−8.52	−8.87
MCF-7:WS8	1 wk		−10.01	−11.92	−10.81	−9.80	−9.01
T47D:A18	1 wk		−9.33	−11.25	−10.01	−8.98	−8.87
BT-474	1 wk		-	−11.31	-	-	−8.71
ZR-75-1	1 wk		-	−11.39	-	-	−8.21
Ishikawa	1 wk		-	−10.97	-	−8.26	−8.57

Transient Transfection and Dual Luciferase Reporter Assays. Ishikawa cells were seeded into 24-well plates at a density of 100,000 cells/well. After 24 hours, cells were transfected with 28.8 μg of pERE(5X)TA-ffLuc and 9.6 μg of pTA-srLuc reporter plasmids using 3 μl of TransIT-LT1 transfection reagent (Mirus Biolabs, Madison, WI) per 1 μg of plasmid DNA in 52.5 ml of OPTI-MEM serum-free media (Invitrogen, Carlsbad, CA). Transfection mix containing the transfection complexes was added to cells in growth media to a final concentration of 0.3 μg pERE(5X)TA-ffLuc and 0.1 μg of pTA-srLuc reporter plasmids per well. After 18 hours, transfection reagents were removed, and fresh media were added instead. After 24 hours post-transfection, cells were treated with test compounds (E_2, E_4, BMI-135, BPTPE, and endoxifen) for 24 hours. After 24-hour treatment, cells were washed once with cold Dulbecco's phosphate-buffered saline (DPBS) (Invitrogen) and lysed, and the estrogen-responsive element (ERE) luciferase activity was determined using Dual-Luciferase Reporter Assay System (Promega, Madison, WI) according to manufacturer's instructions. Samples were quantitated on a Synergy H1 plate reader (BioTek Instruments Inc., Winooski, VT) in white-wall 96-well plates (Nalge Nunc International, Rochester, NY).

Chromatin Immunoprecipitation Assays. The chromatin immunoprecipitation (ChIP) assay was performed as previously described (Sengupta et al., 2010; Obiorah et al., 2014). The antibodies used for the pull-downs were anti-ERα clone F-10X mouse monoclonal (2 μg/μl; 5 μg per reaction) (Santa Cruz Biotechnology), anti–steroid receptor coactivator 3 (SRC-3) clone AX15.3 mouse monoclonal (1 μg/μl; 5 μg per reaction) (Abcam, Cambridge, UK), and normal mouse IgG as intraperitoneal negative control (2 μg/μl; 5 μg per reaction) (Santa Cruz Biotechnology). The DNA fragments were purified using Qiaquick polymerase chain reaction (PCR) purification kit (Qiagen, Germantown, MD). Then, 2 μl of eluted DNA was used for RT-PCR analysis. The primer sequences used were GREB1 proximal ERE enhancer site amplification: 5′-GTGGCAACTGGG TCATTCTGA-3′ sense and 5′-CGACCCACAGAAATGAAAAGG-3′ antisense (Integrated DNA Technologies). The data are expressed as percent input of starting chromatin material after subtracting the percent input pull-down of the intraperitoneal negative control.

Docking of BMI-135 to ERα. The experimental complex structure of TTC-352:ERα was employed for docking BMI-135:ERα because BMI-135 could not crystallize with the ER ligand-binding domain (LBD). The structure was prepared using Maestro software (Schrödinger Release 2019-3; Schrödinger, LLC, New York, NY, 2019) and Protein Preparation Wizard (Schrödinger Release 2019-3: Epik, Impact, Prime; Schrödinger, LLC, 2019). Briefly, the workflow involves the following steps: addition of hydrogen atoms, correction of bonds and bond order assignments, deletion of water molecules beyond 5 Å of a heteroatom, generation of ionization states at pH 7.4, and, finally, the restrained refinement of the ligand-receptor complex. The polar amino acids Asp, Glu, Arg, and Lys were modeled as charged and all Tyr were modeled as neutrals. The ligand was prepared for simulation using the LigPrep module (Schrödinger Release 2019-3; Schrödinger, LLC, 2019) in default settings. The experimental structure of ERα in complex with E_2 was resolved with Tyr537 mutated to Ser. Since all biologic experiments were performed against the WT receptor, we modeled the experimental structure by mutating Ser537 to Tyr using the Maestro software. Then, the residues within a range of 5 Å of Tyr537 were refined while the remaining protein-ligand complex was kept frozen. The ligand was docked to the active site of WT ERα using Induced Fit Docking (Schrödinger Release 2019-3: Glide, Prime; Schrödinger, LLC, 2019) based on Prime and Glide docking (Sherman et al., 2006a,b). This methodology takes into account the receptor's flexibility, allowing the side-chain and backbone movements in the binding site to better adjust to the shape and binding mode of the ligand. The grid was centered on the cocrystallized ligand, and the receptor van der Waals radii of the heavy atoms were scaled down to 0.5. The residues within 5 Å of ligand poses were selected to be refined. The extraprecision option was selected for docking. The top 20–ranked ligand-receptor structures were retained, and the best docking solution was selected based on the Induced Fit Docking score and visual inspection.

Molecular Dynamics Simulations. Molecular dynamics (MD) simulations for the selected BMI-135:ERα complex were carried out with Desmond software (Schrödinger Release 2019-3, Schrödinger, LLC, 2019), utilizing the methodology previously described (Maximov et al., 2020). Briefly, the System Builder module of Desmond was used to solvate the ligand:receptor complex in a periodic orthorhombic water box based on the transferable intermolecular potential with 3 points (TIP3P) model. The charge neutrality of the system was guaranteed by adding sodium and chloride ions. To relax and equilibrate the system, Desmond's default relaxation protocol was employed. Minimization was followed by 50-nanosecond MD production run performed in periodic boundary conditions in the isothermal–isobaric (NPT) ensemble at constant pressure and temperature of 1 atm and 300 K, respectively. The integration time step and the recording interval of coordinates were set to 2 femtoseconds and 2 picoseconds, respectively. Trajectory analysis was carried out using the analysis tool Simulation Integration Diagram of Maestro. The root-mean-square deviation (RMSD) and root-mean-square fluctuation (RMSF) of the receptor backbone atoms relative to the reference structure were calculated and compared with the same metrics computed for the trajectories of ERα bound to E_2 and BPTPE, respectively [previously published (Maximov et al., 2020)]. The clustering algorithm of Desmond was used to extract the most representative frames of trajectory in terms of the conformational space sampling. The trajectory was clustered, the top 10 most-populated clusters were retained, and the representative structure of each cluster was extracted. Then, free binding energy calculations were performed with the Molecular Mechanics/Generalized Born Surface Area (MM-GBSA) method implemented in Schrödinger 2019-3 to select the best structure for analysis and comparison with the E_2 complex. Moreover, protein-ligand interactions (e.g., H-bonds and hydrophobic contacts) were monitored throughout the simulation. All graphs were prepared using the ggplot package of R software (R, version 3.2.3; The R Foundation, Vienna, Austria, 2015), and the figures were generated using PyMol 2.0 (Schrödinger, LLC, 2019).

Human Unfolded Protein Response RT^2 PCR Profiler PCR Arrays (Real-Time Profiler Assay). MCF-7:5C cells were seeded into six-well plates at a density of 200,000 cells/well for the 48- and 72-hour time points and 45,000 cells/well for day-7 time point. After 24 hours, cells were treated with test compounds (E_2, E_4, BMI-135, and BPTPE). Cells were harvested using Qiazol reagent (Qiagen, Hilden, Germany), and total RNA was isolated using an miRNeasy Mini Kit (Qiagen) according to manufacturer's instructions. During the RNA purification process, samples were treated with DNase using the RNase-Free DNase Set (Qiagen) according to manufacturer's instructions. The cDNA was reverse-transcribed using 2 μg of isolated RNA and the High Capacity cDNA Reverse Transcription Kit (Applied Bioscience, Carlsbad, CA) according to manufacturer's instructions. The cDNA was diluted 1:50, and a 2x RT^2 SYBR Green Mastermix (Qiagen) was used to prepare the reactions. The plates were loaded and run on a QuantStudio 6 Flex Real-Time PCR thermocycler (Applied Bioscience) according to manufacturer's instructions. The Ct values were exported at the end of each run, compiled, and uploaded to Qiagen's Data Analysis Center for analysis. For the volcano plots, the fold change [2^(−ΔΔCT)] in the normalized gene expression [2^(−ΔCT)] in the test sample divided the normalized gene expression [2^(−ΔCT)] in the control sample. Fold regulation represents fold-change results in a biologically meaningful way. Fold-change values greater than one indicate a positive regulation or an upregulation, and the fold regulation is equal to the fold change. Fold-change values less than one indicate a negative regulation or down-regulation, and the fold regulation is the negative inverse of the fold

change. The P values of the volcano plots were calculated using a Student's t test of the replicate 2^(−ΔCT) values for each gene in the control group and treatment groups.

Live Cell Imaging and Analysis. MCF-7:5C cells were seeded into 15 μ-slide two-well chambered coverslip slides (Ibidi, Martinsried, Germany) at a density of 300,000 cells/well for the 48-hour time point and at 200,000 cells/well for the 72-hour time point. After 24 hours, cells were treated with test compounds (E_2, E_4, BMI-135, and thapsigargin). On the day of live cell imaging, the green fluorescent dye ThT (UPR-indicative dye) (Sigma-Aldrich) was freshly prepared as previously described (Beriault and Werstuck, 2013), and the blue fluorescent live cell nuclear dye Hoechst 33342 (counterstain dye) (Thermo Fisher Scientific) was freshly prepared at a final concertation of 5 μg/ml. The staining with ThT was for 1 hour, and this was followed by substituting the culture media (containing test compounds and ThT) with PBS containing Hoechst 33342 for 15 minutes in a CO_2 incubator. Fluorescent images of MCF-7:5C live cells were taken at a 38-millisecond exposure under a 20×/0.7 objective with ZEISS Celldiscoverer 7 (Carl Zeiss AG, Oberkochen, Germany). Images were converted to 12-bit before being quantified by the ZEISS Zen Software Module-Image Analysis. Cells from each image were manually counted to normalize the fluorescent data per cell. Relative intensity per cell = ThT intensity/cell count and was generated for each treatment per image. A mean of the relative intensity per cell (using three images per treatment) was then calculated to give a final quantification alongside the S.D. The relative intensity per cell data are represented in Table 2. The excitation and emission settings were Hoechst 33342 (Excitation: 348 nm, Emission: 455 nm) and ThT (Excitation: 433 nm, Emission: 475 nm).

Annexin V–Staining Assays. MCF-7:5C cells were seeded into 10-cm Petri dishes at a density of 800,000 cells/dish for the 72- and 96-hour time points. MCF-7:2A cells were seeded into 10-cm Petri dishes at a density of 400,000 cells/dish for day-9 time point and at 100,000 cells/dish for day-13 time point. MCF-7:RAL cells were seeded into 10-cm Petri dishes at a density of 150,000 cells/dish for day-14, day-17, and day-21 time points. After 24 hours, cells were treated with test compounds (E_2, E_4, BMI-135, BPTPE, 4OHT, endoxifen, raloxifene, ICI, GSK G797800, and MKC-3946). Harvested cells were suspended in 1× binding buffer, and 1×10^5 cells were stained simultaneously with FITC-labeled annexin V and propidium iodide (PI) for 15 minutes at 37°C using the FITC Annexin V Apoptosis Detection Kit I (BD Pharmingen, San Diego, CA) according to the manufacturer's instructions. The cells were analyzed using a BD Accuri C6 plus flow cytometer.

Statistical Analyses. All data are mean ± S.D. of three different fields for each condition from three independent biologic experiments performed in technical duplicates. One-way ANOVA was used with a follow-up Tukey's test to determine the statistical significance of the treatments.

TABLE 2

Quantification of the UPR in live MCF-7:5C cells through measuring ThT relative intensity/cell

(A) ThT relative intensity/cell (mean and S.D.) with test compounds after 48-hour treatments. (B) ThT relative intensity/cell (mean and S.D.s) after 72-hour treatments. This reflects the differential capacity of test compounds in inducing EnR stress over time. ThT relative intensity/cell per treatment is representative of three biologic repeats.

Compound	(A) Day 2 Relative Intensity/Cell (Mean)	S.D.
Veh	0.276	0.052
Thapsigargin	0.875	0.061
E_4	1.245	0.073
E_2	0.741	0.097
BMI-135	0.497	0.047
	(B) Day 3	
Compound	Relative Intensity/Cell (Mean)	S.D.
Veh	0.296	0.057
Thapsigargin	10.055	0.068
BMI-135	4.878	0.049

Results

Effects of E_4 and BMI-135 on Cell Viability and Proliferation in Numerous BC Models. Cell viability and proliferation assays were used to investigate the biologic properties of test compounds. Estetrol and ShERPA BMI-135 display activity similar to E_2 but right shifted across eight BC cell lines that are estrogen-dependent (MCF-7:WS8, T47D:A18, MCF-7:PF, BT-474, and ZR-75-1), estrogen-independent (MCF-7:5C, MCF-7:2A, and MCF-7:RAL), endocrine-sensitive (MCF-7:2A), endocrine-resistant (MCF-7:PF, MCF-7:5C, and MCF-7:RAL), mutant p53 (T47D:A18), human epidermal growth factor receptor 2–positive (BT-474), luminal A (ZR-75-1), and luminal B (BT-474).

The concentration 1 μM for E_4 and BMI-135 achieved either the maximal cellular growth (Fig. 2, A–E; Supplemental Fig. 1, A–C), or the maximal cellular death (Fig. 2, F–H; Supplemental Fig. 1, D–F). Both were shown to be less potent full agonists compared with E_2, requiring higher concentrations to produce the same maximal effect of E_2. The EC_{50} for all test compounds used in treating these cell lines are summarized in Table 1.

In MCF-7:5C, E_4 and BMI-135 almost completely reduced the amount of viable MCF-7:5C cells after 1 week of treatment in a dose-dependent manner, with a maximum reduction of cells by an average of 58% for E_4 and 46% for BMI-135 at their highest concentration of 10^{-6} M ($P < 0.05$ compared with vehicle) (Fig. 2F). Reduction in the amount of viable MCF-7:5C cells by E_2 at 10^{-9} M was by an average of 58% (Fig. 2F). In MCF-7:2A, E_4 and BMI-135 almost completely reduced the amount of viable MCF-7:2A cells after a 2-week treatment in a dose-dependent manner, with a maximum reduction of cells by an average of 57% for E_4 and 50% for BMI-135 at their highest concentration of 10^{-6} M ($P < 0.05$ compared with vehicle) (Fig. 2G). Reduction in the amount of viable MCF-7:2A cells by E_2 at 10^{-9} M was by an average of 67% (Fig. 2G). In MCF-7:RAL, E_4 and BMI-135 almost completely reduced the amount of viable MCF-7:RAL cells after a 3-week treatment in a dose-dependent manner, with a maximum reduction of cells by an average of 45% for E_4 and 43% for BMI-135 at their highest concentration of 10^{-6} M ($P < 0.05$ compared with vehicle) (Fig. 2H). Reduction in the amount of viable MCF-7:RAL cells by E_2 at 10^{-9} M was by an average of 45% (Fig. 2H).

Effects of E_4 and BMI-135 Are Mediated via ERα. MCF-7:5C, MCF-7:2A, and MCF-7:RAL representing LTED estrogen-independent BC were treated with 1 μM E_4, 1 μM BMI-135, and a combination of these with 1 μM 4OHT and 1 μM endoxifen to investigate whether E_4 and BMI-135 exert their function via ERα. In MCF-7:5C, full estrogen agonists should cause cellular death within 1 week, antagonists should not (i.e., MCF-7:5C is endocrine-resistant), and the agonists' pairing with the antagonists should block the death effect. Indeed, E_2, E_4, and BMI-135 killed the cells within 1 week ($P < 0.05$ compared with vehicle) (Supplemental Fig. 2A), whereas 4OHT and endoxifen did not ($P < 0.05$ compared with vehicle) (Supplemental Fig. 2A). The combination of E_2, E_4, and BMI-135 with 4OHT and endoxifen blocked the death effect (Supplemental Fig. 2A).

In MCF-7:2A, full agonists should cause cellular death within 2 weeks, antagonists should cause growth inhibition

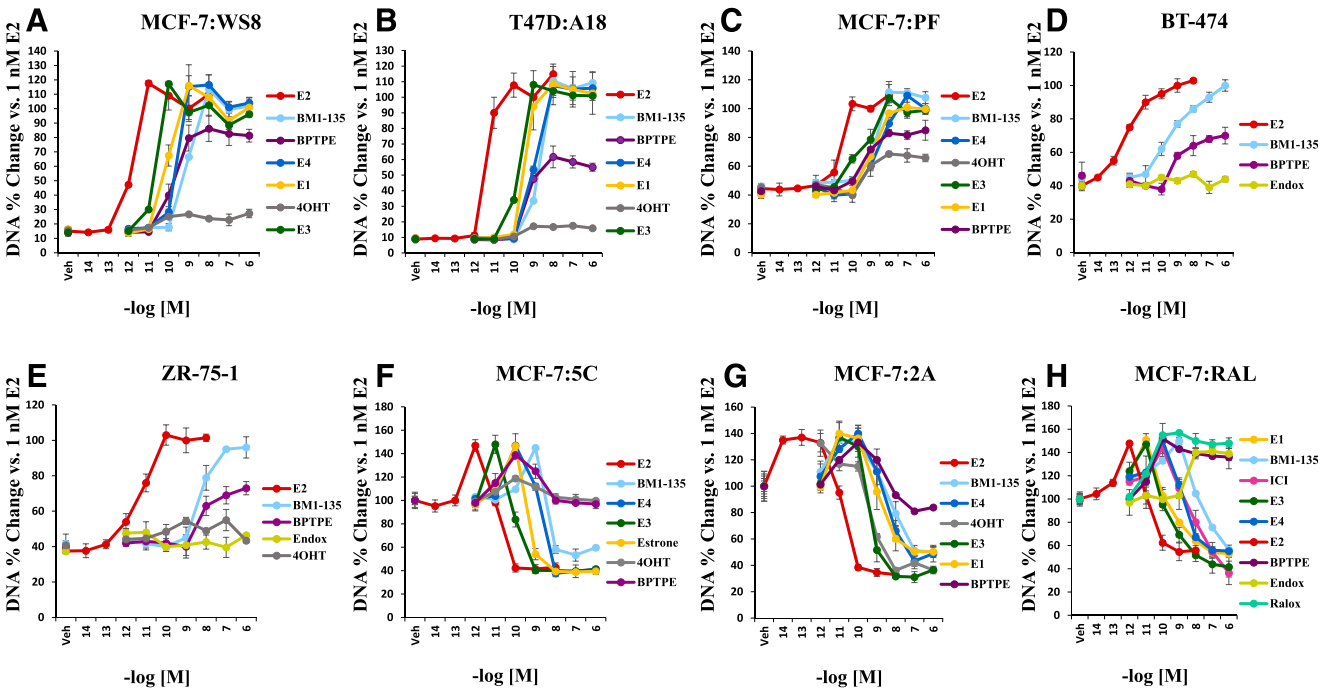

Fig. 2. Cell viability and proliferation assays in multiple BC cell lines with test compounds. (A) Effects of test compounds alone after 7 days of treatment (percent DNA of vehicle vs. test compounds' concertation) in MCF-7:WS8. (B) Effects of test compounds alone after 7 days of treatment in T47D:A18. (C) Effects of test compounds alone after 7 days of treatment in MCF-7:PF. (D) Effects of test compounds alone after 7 days of treatment in BT-474. (E) Effects of test compounds alone after 7 days of treatment in ZR-75-1. (F) Effects of test compounds alone after 7 days of treatment in MCF-7:5C. (G) Effects of test compounds alone after 14 days of treatment in MCF-7:2A. (H) Effects of test compounds alone after 21 days of treatment in MCF-7:RAL. Endox, endoxifen.

(i.e., MCF-7:2A is endocrine-sensitive), and the agonists' pairing with the antagonists should block the death effect. Indeed, E_2, E_4, and BMI-135 killed the cells within 2 weeks ($P < 0.05$ compared with vehicle) (Supplemental Fig. 2B), whereas 4OHT and endoxifen caused growth inhibition ($P < 0.05$ compared with vehicle) (Supplemental Fig. 2B). The combination of E_2, E_4, and BMI-135 with 4OHT and endoxifen blocked the death effect (Supplemental Fig. 2B).

In MCF-7:RAL cells, full agonists should cause cellular death within 2 to 3 weeks in vitro; antagonists, especially Selective ER Modulator (SERM) raloxifene (positive control), should cause cellular growth; and the agonists' pairing with antagonists should block the death effect. Indeed, E_2, E_4, and BMI-135 killed the cells within 3 weeks ($P < 0.05$ compared with vehicle) (Supplemental Fig. 2C), whereas the SERMs 4OHT, endoxifen, and especially raloxifene caused cellular growth ($P < 0.05$ compared with vehicle) (Supplemental Fig. 2C). The combination of E_2, E_4, and BMI-135 with 4OHT and endoxifen blocked the death effect (Supplemental Fig. 2C). Interestingly, ICI (a selective ER downregulator or "pure antiestrogen") caused a decrease in cell DNA amount in MCF-7:RAL cells after a 3-week treatment ($P < 0.05$ compared with vehicle) (Supplemental Figs. 1F and 2C).

Endoxifen, the major biologically active metabolite of TAM, was used as an antiestrogenic control alongside 4OHT and neither induced an increase or decrease in viable cells ($P < 0.05$ compared with vehicle controls) (Supplemental Fig. 2A). Only in MCF-7:2A cells did 4OHT and endoxifen cause growth inhibition (Supplemental Fig. 2B), and in MCF-7:RAL cells, both caused growth stimulation (Supplemental Fig. 2C), as predicted.

BMI-135 Induces the Transcriptional Activity of ERα Similar to E_2 in WT MCF-7:WS8 and Apoptotic-Type MCF-7:5C BC Models. Quantitative RT-PCR was used to assess the transcriptional activity of ERα on ERE genes (*TFF1* and *GREB1*) with test compounds. After 24-hour treatment in MCF-7:WS8 cells, BMI-135 increased the levels of *TFF1* and *GREB1* mRNAs compared with vehicle controls ($P < 0.05$) (Fig. 3, A and B). On the other hand, the partial agonist BPTPE induced a partial increase in the levels of *TFF1* and *GREB1* mRNAs and less than that of full agonist E_2 ($P < 0.05$) and BMI-135 ($P < 0.05$) (Fig. 3, A and B). The minimal concentration that produced a complete increase in the levels of *TFF1* and *GREB1* was at 10^{-6} M for BMI-135 ($P < 0.05$ compared with vehicle) (Fig. 3, A and B).

After 24-hour treatment in MCF-7:5C cells, BMI-135 increased the levels of *TFF1* and *GREB1* mRNAs compared with vehicle controls ($P < 0.05$) (Fig. 3, C and D). On the other hand, BPTPE induced a partial increase in the levels of *TFF1* and *GREB1* mRNAs and less than that of E_2 ($P < 0.05$) and BMI-135 ($P < 0.05$) (Fig. 3, C and D). The minimal concentration that produced a complete increase in the levels of *TFF1* and *GREB1* was at 10^{-6} M for BMI-135 ($P < 0.05$ compared with vehicle) (Fig. 3, C and D).

The ERE-dependent transcriptional activity with E_4 was done by Abot et al. (2014) and showed an induction similar to E_2, only with a lower potency.

Overall, the induction of the mRNA levels of *TFF1* and *GREB1* by BMI-135 in MCF-7:WS8 and MCF-7:5C was similar to that by full agonist E_2, only at a lower potency.

Estetrol and BMI-135 Induce the Transcriptional Activity of ERα Similar to E_2 in Human Endometrial Cancer Model Ishikawa. Transient transfection and luciferase activity assays were used to determine the transcriptional activity of ERα on estrogen-responsive genes (*5xERE*) with test compounds as ERE dual luciferase activity. After

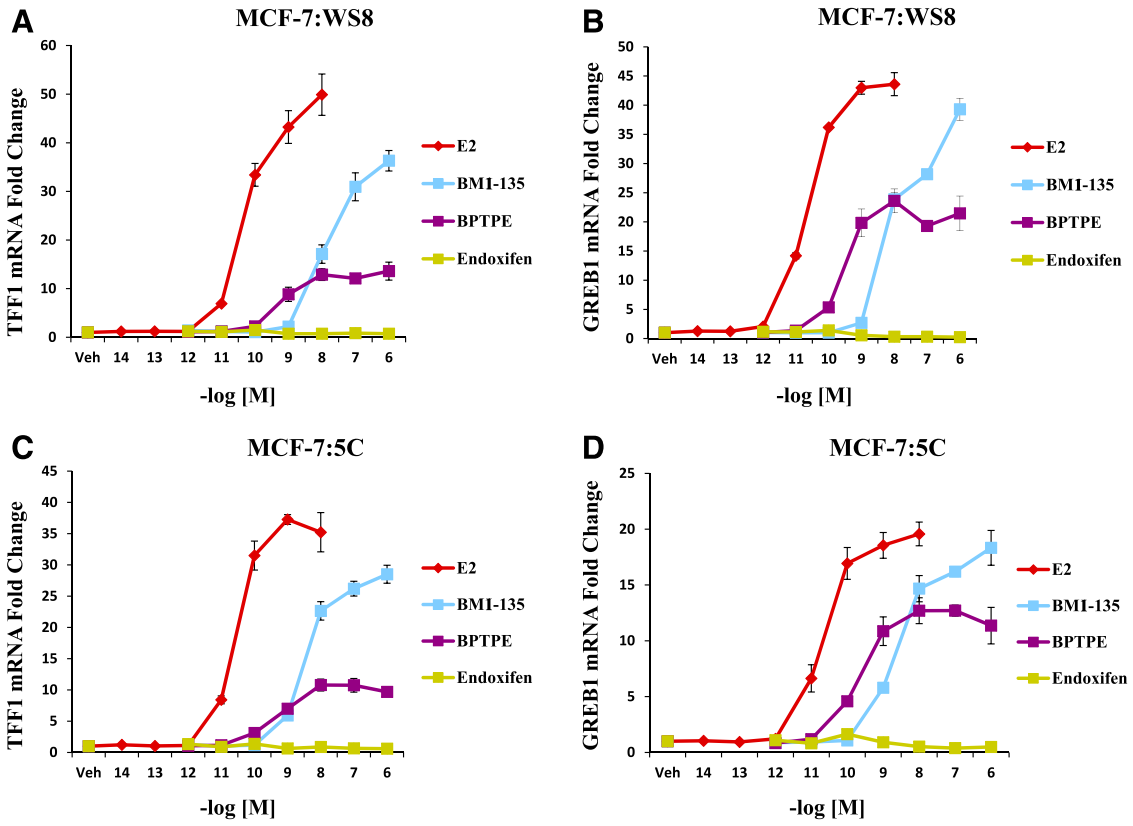

Fig. 3. Transcriptional activity of well characterized estrogen-responsive genes TFF1 (or pS2) and GREB1 in WT MCF-7:WS8 and LTED MCF-7:5C with test compounds. (A) mRNA expression of TFF1 in MCF-7:WS8 cells after 24-hour treatment with 1 nM E_2 and 1 μM for other test compounds. (B) mRNA expression of GREB1 in MCF-7:WS8 cells after 24-hour treatment with 1 nM E_2 and 1 μM for other test compounds. (C) mRNA expression of TFF1 in MCF-7:5C cells after 24-hour treatment with 1 nM E_2 and 1 μM for other test compounds. (D) mRNA expression of GREB1 in MCF-7:5C cells after 24-hour treatment with 1 nM E_2 and 1 μM for other test compounds. Data are mean ± S.D. from three independent experiments performed in triplicate analyzed by one-way ANOVA.

24-hour treatment of Ishikawa cells, E_4 and BMI-135 increased the levels of 5x-ERE luciferase activity compared with vehicle controls ($P < 0.05$) (Fig. 4A). On the other hand, the partial agonist BPTPE induced a partial increase in the levels of 5x-ERE luciferase activity and less than that of full agonist E_2, E_4, and BMI-135 ($P < 0.05$) at concentration range of 10^{-8}–10^{-6} M (Fig. 4A). The minimal concentration that produced a complete increase in the levels of 5x-ERE luciferase activity was at 10^{-7} M for E_4 and BMI-135 ($P < 0.05$ compared with vehicle) (Fig. 4A).

To determine whether the effects of E_4 and BMI-135 were mediated via ERα in Ishikawa cells, transiently transfected

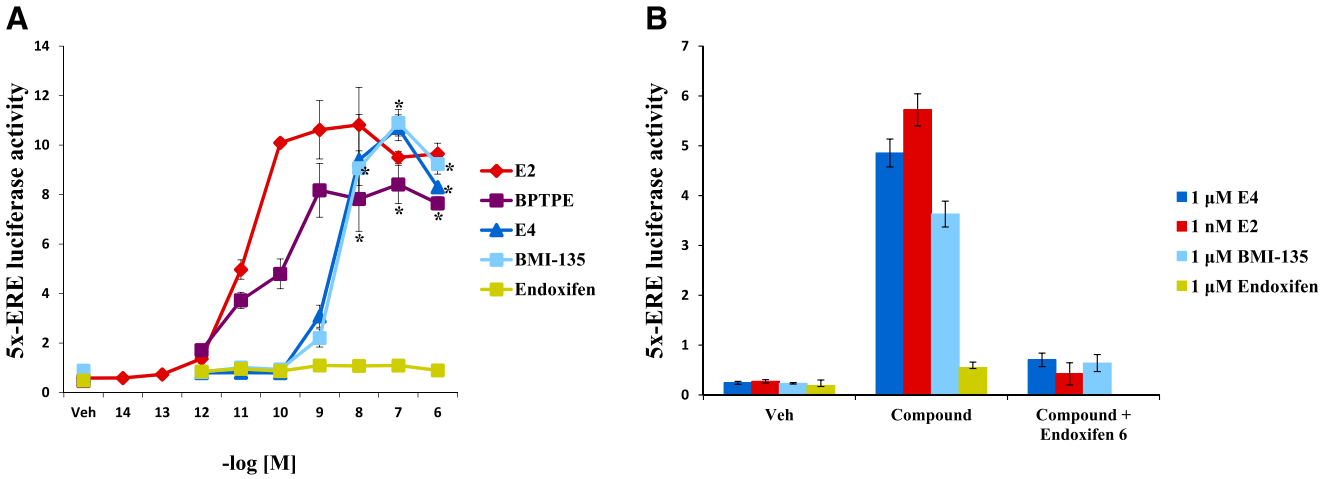

Fig. 4. Transient transfection of the human endometrial cancer cells Ishiskawa with 5x-ERE and dual luciferase activity assay. (A) Dose-response curve of test compounds vs. 5x-ERE luciferase activity (promoter activity = Firefly luciferase activity/*Renilla* luciferase activity). (B) 5x-ERE luciferase activity with indicated test compounds alone vs. in combination with 1 μM endoxifen. Data are mean ± S.D. from three independent experiments performed in triplicate analyzed by one-way ANOVA. *$P < 0.05$: statistical difference between E_4 or BMI-135 and BPTPE treatments over 10^{-8}–10^{-6} concentration range (*t* test). Veh, vehicle.

Ishikawa cells were treated with test compounds in combination with antagonist endoxifen for 24 hours, and luciferase activity assays were conducted (Fig. 4B). The increase in the levels of 5x-ERE luciferase activity with E_4 and BMI-135 was blocked with endoxifen treatment at 10^{-6} M ($P < 0.05$ compared with vehicle) (Fig. 4B). This confirms that E_4 and BMI-135 exert their function via Ishikawa's ERα. In addition, endoxifen alone did not increase the levels of 5x-ERE luciferase activity in Ishikawa cells, acting as an antagonist in this uterine model (Fig. 4B).

Overall, the induction of the levels of 5x-ERE luciferase activity by E_4 and BMI-135 in Ishikawa cells was similar to that by full agonist E_2, only at a lower potency (Table 1).

E_4 and BMI-135 Recruit ERα and SRC-3 to the *GREB1* Proximal Enhancer Region Similar to E_2 in MCF-7:5C BC Model. ChIP assays were used to assess the recruitment of ERα and SRC-3 to the *GREB1* proximal enhancer region with test compounds. Estetrol and BMI-135 treatments resulted in a very strong recruitment of ERα to the *GREB1* proximal enhancer region similar to E_2 and higher than that with the partial agonist BPTPE ($P < 0.05$) (Fig. 5A).

However, the recruitments of the coactivator SRC-3 to the *GREB1* proximal enhancer region with E_4 and BMI-135 treatments were higher than that with BPTPE ($P < 0.05$) (Fig. 5B). SRC-3 recruitment with E_2 was the highest. With E_4, there was an 18.72% recruitment reduction compared with E_2; with BMI-135, there was a 51.17% recruitment reduction compared with E_2; with BPTPE, there was a 65.47% recruitment reduction compared with E_2; and with endoxifen, there was a 98.14% recruitment reduction compared with E_2 (Fig. 5B).

Overall, the recruitment of ERα to the *GREB1* proximal enhancer region with E_4 and BMI-135 in MCF-7:5C cells was similar to that by full agonist E_2, and the recruitment of SRC-3 to the *GREB1* proximal enhancer region with E_4 and BMI-135 in MCF-7:5C cells was higher than that with the partial agonist BPTPE. Although SRC-3 recruitment with BMI-135 treatment was lower than that with E_2 ($P < 0.05$), it was higher than that with BPTPE ($P < 0.05$).

Analysis of E_4 and BMI-135's Binding Mode in Comparison with Full Agonist E_2 and Partial Agonist BPTPE. To outline the similarities and differences between BMI-135 and other investigated ligands (e.g., E_2, E_4, and BPTPE), their overall conformations and interactions with residues of the binding site were analyzed (Fig. 6; Supplemental Fig. 10, B–I). The BMI-135 ligand was docked into the experimental structure of the ERα:TTC-352 complex and adopted the canonical agonist conformation with helix 12 (H12) positioned over the binding pocket, sealing the ligand inside. We used the induced fit docking methodology because it allows flexibility for certain parts of the receptor (e.g., amino acids of the binding site). The top-ranked BMI-135–receptor pose and experimental structures of ERα bound to E_2, E_4, and BPTPE adopt the agonist conformation of ERα, with H12 sitting in a groove between H5 and H11 delineated by H3 and the ligands occupying the binding pocket composed of residues from helices H3, H6, H8, and H11 (Fig. 6, A, C, and E).

The predicted binding mode of BMI-135 shared, to some extent, the network of interactions specific to E_2, E_4, and BPTPE, as shown (Fig. 6, B, D, and F; Supplemental Fig. 10, F–I). The familiar H-bond network between a phenolic hydroxyl, Glu353, and Arg394 was common to ligands. The benzothiophene moiety of BMI-135 was implicated in π-π stacking interactions with Phe404 and made several additional contacts with Ala350 (H3), Leu387, Met388, and Leu391 (H6), similar to A and B rings of E_2. The two substituted phenyl rings were involved in hydrophobic contacts with Leu346 (H3), Ala350 (H3), Ile424 (H8), and Leu525 (H11), and the fluorine substituent was headed toward Thr347 (H3). The most apparent difference between BMI-135 and E_2 binding modes (also seen for BPTPE) was the absence of H-bond with the imidazole ring of His524. We noticed that the side chain of His524 was pushed toward the outer part of the protein by the bulkier ethinyl group of BMI-135, which hovered between helices H3, H8, and H11 in a space delineated by residues Met343 (H3), Val418 (H8), Met421 (H8), Leu525 (H11), and Met528 (H11) (Supplemental

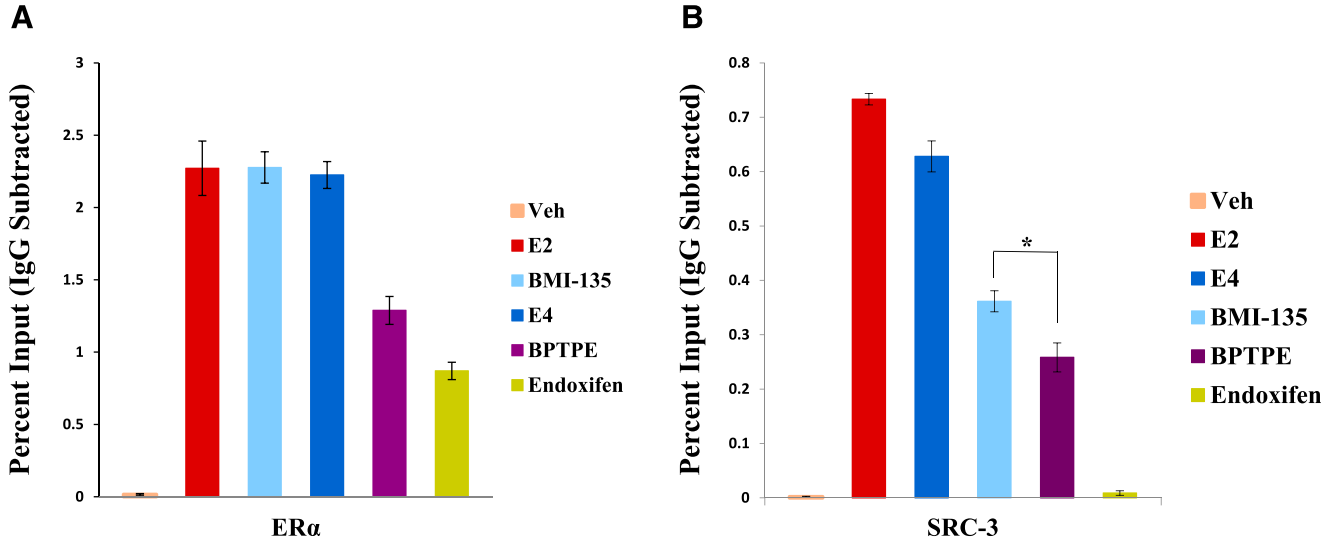

Fig. 5. ChIP assay in MCF-7:5C cells showing the recruitment of ERα and coactivator SRC-3 to TFF1 ERE promoter. Recruitment of ERα (A) and SRC-3 (B) after 45-minute treatment with indicated ligands; 1 nM E_2 and 1 μM for the rest of test compounds. Recruitment of ERα and SRC-3 was calculated as percentage of the total input after subtracting the IgG recruitment. All treatments were performed in triplicate; data represent the average of these replicates. *$P < 0.05$: statistical difference between BMI-135 and BPTPE treatments with SRC-3 recruitment. Veh, vehicle.

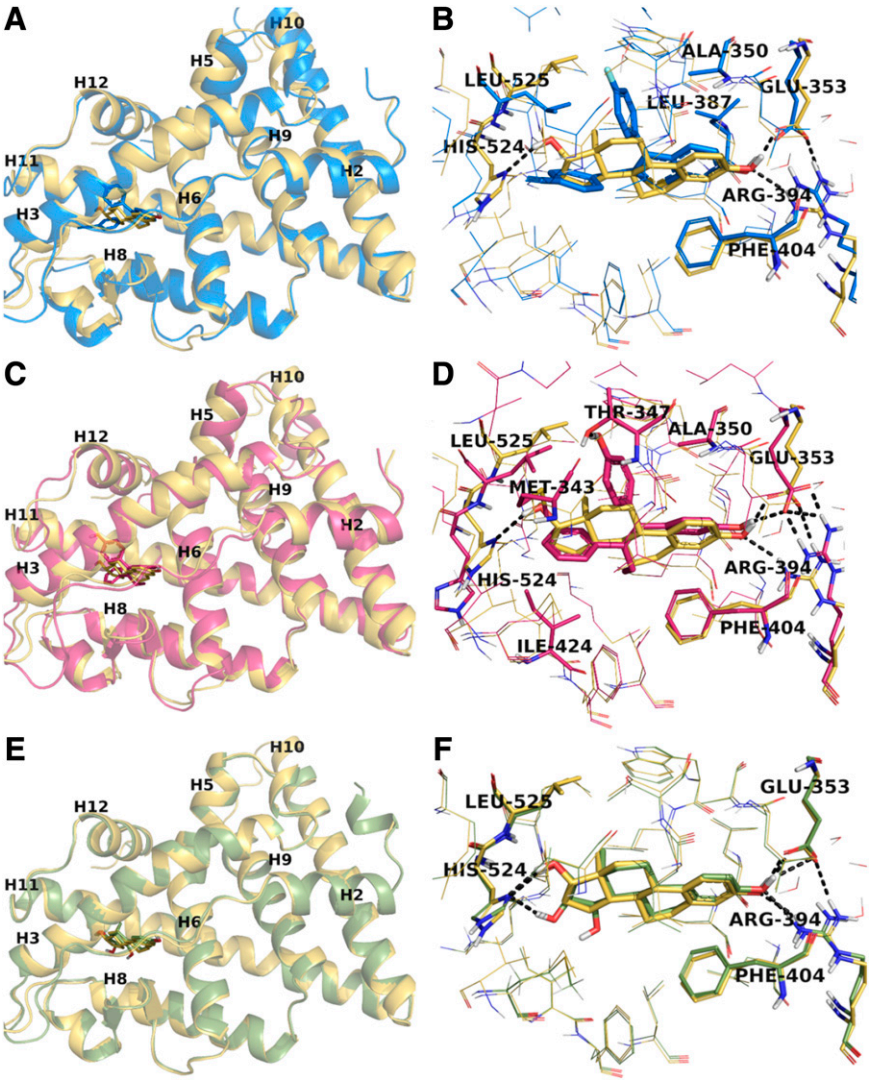

Fig. 6. Representations of ERα-LBD with E_2, E_4, BMI-135, and BPTPE. Comparison between the agonist conformation of ERα-LBD in complex with E_2, superimposed with BMI-135 (A), BPTPE (C), and E_4 (E) in similar conformations of the receptor. The helices forming the ligand-binding site are labeled together with helix 12 (H12), which defines the receptor conformation and those essential for the coactivator binding groove. The alignment in the binding site and the contacts between BMI-135 (B), BPTPE (D), E_4 (F), and critical amino acids of the binding pocket are revealed in comparison with the binding alignment of E_2. For BMI-135 and BPTPE, the most representative conformations extracted from MD trajectories are shown, whereas for E_2 and E_4, the experimental structures are presented. The ligand: receptor complexes are colored based on C atoms as follows: yellow for E_2, blue for BMI-135, magenta for BPTPE, and light green for E_4, whereas the N, O, and S atoms are colored in dark blue, red, and yellow, respectively. For clarity, the amino acids involved in critical contacts (i.e., H-bonds and π- π stacking) are shown as sticks together with those having contacts with occurrence frequencies during the MD trajectories larger than 40% of the simulation time. The remaining amino acids of the binding sites are shown as lines. The H-bonds redepicted as black dashed lines.

Fig. 10H). These flexible residues permitted the accommodation of the large etinylbenzoyl moiety in this part of the binding pocket.

A contact unique to BPTPE was the H-bond between the second phenolic group of the ligand and the OH group of Thr347 (Fig. 6D), whereas specific to E_4 was the involvement of the second OH group of the D ring into an extra H-bond to His524, adding stability to the ligand in the binding site (Fig. 6F). In addition, the hydrophobic contacts and π-π stacking interactions with Phe404 complemented the binding profile of these ligands (Supplemental Fig. 10, C, E, G, and I).

MD Simulations Analysis. To investigate the stability of BMI-135 in the binding site of ERα, the dynamics of the interactions, and how they compared with the interactions in the structures of E_2 and BPTPE, we performed MD simulations against the top-ranked ERα:BMI-135 complex, as previously described in *Materials and Methods*. The recorded trajectory was analyzed and compared with the trajectories previously reported (Maximov et al., 2020) for WT ERα bound to E_2 and BPTPE.

Firstly, we explored the conformational stability of the simulation. To ensure that the model had reached equilibrium, RMSDs of the protein backbone atoms, relative to their position in the first frame, were computed for trajectory. The RMSD evolution indicated that the system had reached equilibrium after approximately 5 nanoseconds, similar to the E_2 model (Supplemental Fig. 3A).

Next, to investigate the mobility of the protein and the dynamics of ligand binding, we monitored the RMSF of the residues along the trajectory (Supplemental Fig. 3A). Comparing the RMSF calculated for backbone atoms with the previously reported values for the runs of E_2 and BPTPE, we noticed a similar pattern for BMI-135 and E_2. There were several substantial fluctuations, which mainly overlapped with the flexible domains of the receptor (a significant peak located between residues 332–338 matches the loop connecting helices H2 and H3). The largest peak in all trajectories was situated between residues 456 and 469, part of the loop connecting H9 to H10, and missing in all experimental structures used in this analysis (Supplemental Fig. 3A). The high flexibility of this domain and the predicted coordinates for this loop could explain the observed fluctuation. Overall, the BMI-135 complex showed mobility domains matching with the E_2 system mainly positioned in connection loops, flexible regions of a protein. In addition, based on the previous analysis of the correlation between RMSF values and

B-factors for E_2 and BPTPE, we observed that the high RMSF values of protein fragments parallel with large B-factors.

Then, we explored the stability of the ligands relative to the protein and the binding site together with the internal fluctuations of ligands' atoms (Supplemental Fig. 3B). The analysis shows that BMI-135 did not fluctuate significantly and was stably bound in the active site, similar to E_2 and BPTPE, with average RMSD values of 0.8 ± 0.23 and 1.6 ± 0.34 Å, respectively (Supplemental Fig. 3B).

Analysis of BMI-135 Ligand-Protein Interactions in Modeled WT ERα Systems. We analyzed the binding dynamics of BMI-135 and assessed the stability of the interactions by monitoring the frequency of occurrence of that specific interaction throughout the trajectory. Overall, the computed variations of RMSF, based on the backbone and side-chain atoms, showed similar trends for E_2, BMI-135, and BPTPE (Supplemental Fig. 10A). The residues involved in H-bonds with the ligands (e.g., Thr347, Glu353, His524), π-π stacking, and hydrophobic contacts (e.g., Phe404, Ala350, Leu387) showed RMSF values that were smaller than average and fluctuated less, indicating stable contacts. This observation was also supported by the occurrence frequencies of these interactions monitored throughout the trajectory (Supplemental Fig. 11, A–C). A striking difference was noticed for BMI-135, which displayed the largest peak of side-chain RMSF for Arg394. This mobility indicated that Arg394 was not involved in a direct H-bond with the ligand and/or ionic bridges to Glu353, therefore not stabilizing it. However, H-bonds were sporadically monitored during the simulation between the ligand and Arg394 via a water bridge, with frequencies below 15%. Additionally, the bulkier substituents of BMI-135 displaced the amino acid and forced it not to adopt orientations proper for the binding.

Similarly to E_2, BMI-135 was stabilized by the H-bond to Glu353 and π-π stacking interactions with Phe404 but occurred in lower frequency. The hydrophobic contacts, mainly with residues Ala 350, Leu384, Leu 387, Met388, Leu391, Leu403, and Leu525, were stable for both ligands during the simulation time, however, in lower occurrence frequencies for BMI-135 (Supplemental Fig. 11, A and B). The H-bond to His524, which was very stable for E_2, was lacking for BMI-135 and BPTPE, but occasional hydrophobic contacts with the ethinyl-benzoyl moiety of BMI-135 were noticed. BPTPE mainly recapitulated the interactions mentioned above but with frequencies lower than those of E_2.

A distinctive feature of BPTPE is the H-bonding to Thr347, which occurred in over 95% of the trajectory (Supplemental Fig. 11C), indicating a very stable contact, and this was confirmed by the low RMSF value of the residue (Supplemental Fig. 10A). However, as previously shown, the H-bond to Thr347 prevented the formation of an H-bond between the side chains of Asn348 (H3) and Tyr537 (H11) (usually forming a stabilizing contact in the vicinity of H12) and, together with the phenol group of BPTPE, triggered a slightly different conformation of H12 (Maximov et al., 2020). Although the 4-fluoro-phenyl substituent of BMI-135 was oriented toward Thr347, the interaction Asn348-Tyr537 was not disturbed and occurred 52% of the simulation time but to a slightly lesser extent compared with E_2 (i.e., 70%); nonetheless, it is still significant. Another contact that added stability to the agonist conformation of the receptor was the interaction between the side chain of His524 and backbone of Glu419, which was found almost 80% of the time during the simulation of E_2. Surprisingly, this contact was observed in the trajectory of BMI-135 with a frequency of 72% of the simulation time.

Overall, these data show the confirmation of the BMI-135: ERα complex to be more similar to that of E_2, compared with that of BPTPE.

E_4 and BMI-135 Activate the UPR. Human UPR real-time profiler assays were used to assess the regulation of UPR genes with test compounds. Cell viability and proliferation assays showed a decline in MCF-7:5C cell DNA amount with E_2 and E_4 treatments at 72 hours (Fig. 7D). Furthermore, flow cytometry showed apoptosis at 72 hours (annexin staining 14.8% with E_2 and 12.6% with E_4 vs. vehicle control 4.5%) (Fig. 7E). The time point at 48 hours was chosen to investigate the terminal (or proapoptotic) UPR gene regulation with E_2 and E_4 treatments in MCF-7:5C cells, which precedes apoptosis by 72 hours.

After 48-hour treatment with 1 nM E_2 and 1 μM E_4 [i.e., these concentrations were shown earlier to trigger maximal cellular death (Fig. 2; Table 1)], the endoplasmic reticulum–associated degradation (ERAD) genes (downstream IRE1α/XBP1s and ATF6 p50), HTRA4 ($P < 0.001$), SYVN1 ($P < 0.001$), and HERPUD1 ($P < 0.001$), were downregulated (Fig. 7, B and C; Supplemental Fig. 5, A and B). The lipid or cholesterol metabolism genes (downstream IRE1α/XBP1s and ATF6 p50), MBTPS1 ($P < 0.001$) and SERP1 ($P < 0.001$), were downregulated with E_2 treatment, whereas only MBTPS1 ($P < 0.001$) was downregulated with E_4 (Fig. 7, B and C; Supplemental Fig. 5, A and B). The chaperone (chaperones are usually downstream IRE1α/XBP1s, PERK/P-eIF2α:ATF4, and ATF6 p50) gene SIL1 ($P < 0.001$) was downregulated with E_4 treatment (Fig. 7C; Supplemental Fig. 5B). By contrast, the genes CEBPB ($P < 0.001$) and INHBE ($P < 0.001$), which reflect high UPR stress, were upregulated (Fig. 7, B and C; Supplemental Fig. 5, A and B).

The heat map of MCF-7:5C cells with E_2 and E_4 treatments at 48 hours displays a general UPR gene downregulation (situated on the right side of the heat map) compared with vehicle control (situated on the left) (Fig. 7A). The majority of the profiler assays' genes belong to the lipid metabolism, ERAD, and chaperone gene groups, which are considered prosurvival mechanisms that help the cells cope with extrinsic or intrinsic cellular stress (Fig. 9). This general downregulation by 48 hours (Fig. 7, B and C; Supplemental Fig. 5, A and B) highlights MCF-7:5C cells' proapoptotic UPR phase and programming to undergo apoptosis by 72 hours (Fig. 7E).

Cell viability and proliferation assays showed a decline in MCF-7:5C cell DNA amount with BMI-135 treatment by 96 hours (Fig. 8D). Furthermore, flow cytometry showed apoptosis by 96 hours (annexin staining 17.1% with BMI-135 vs. vehicle control 5.7%) (Fig. 8E). The time point of 72 hours was chosen to investigate the proapoptotic UPR gene regulation with BMI-135 treatment in MCF-7:5C cells, which preceded apoptosis by 96 hours. Another time point of 48 hours was chosen to compare and contrast the UPR gene regulation with that by 72 hours and show how this regulation is dynamic and culminates over time.

After 48-hour treatment with 1 μM BMI-135, the ERAD genes EDEM1 ($P < 0.001$), HTRA4 ($P < 0.001$), SYVN1 ($P < 0.001$), and HERPUD1 ($P < 0.001$) were downregulated (Fig. 8C; Supplemental Fig. 5C). The lipid metabolism genes MBTPS1 ($P < 0.001$) and SERP1 ($P < 0.001$) were downregulated (Fig. 8C; Supplemental Fig. 5C). By contrast, the genes CEBPB ($P < 0.001$) and INHBE ($P < 0.001$) were upregulated (Fig. 8C;

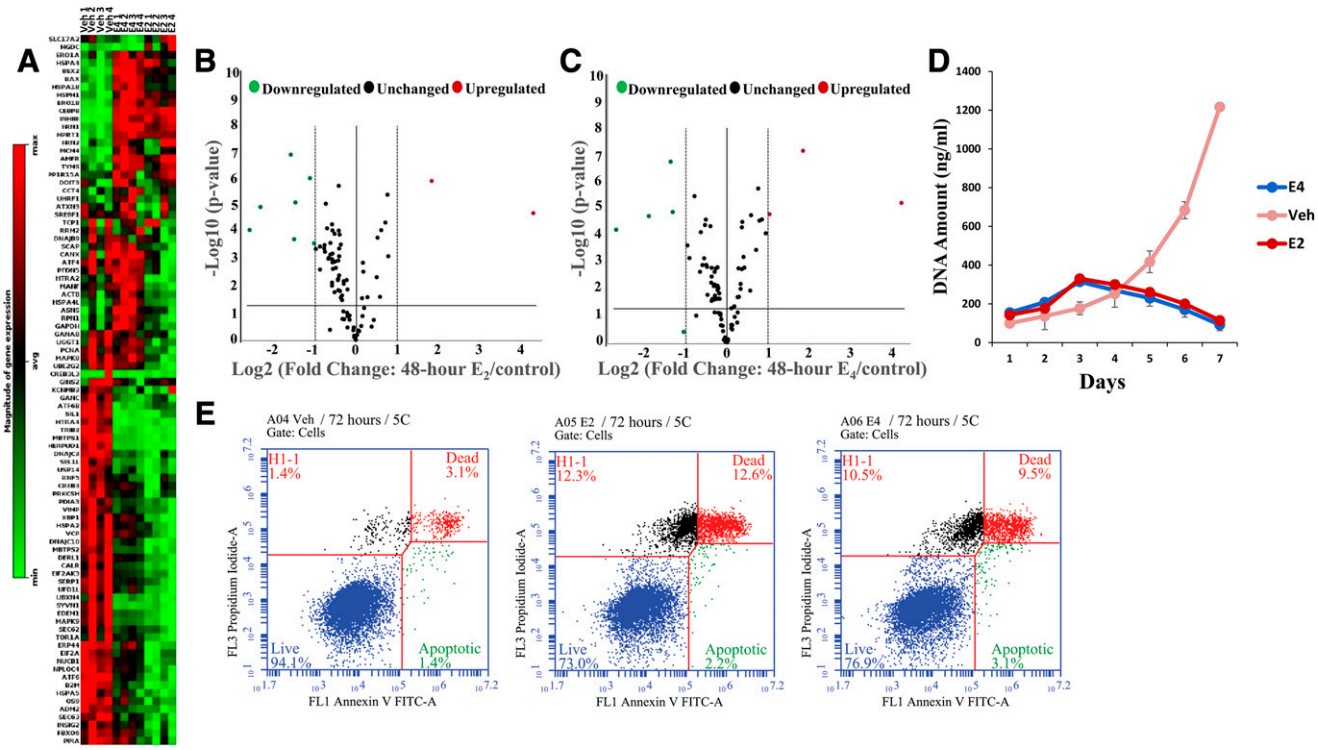

Fig. 7. Human UPR RT^2 PCR profiler PCR arrays, proliferation assays, and annexin V staining in MCF-7:5C cells with 48-hour, 96-hour, and 7-day E_2 and E_4 treatments. (A) A heat map providing a visualization of the fold changes in expression between select groups (from left to right; vehicle, E_4, and E_2, respectively) for every gene in the array in the context of the array layout. (B) A volcano plot of 48-hour E_2 treatment identifying significant gene-expression changes and displaying statistical significance vs. fold change on the *y*- and *x*-axes, respectively. The volcano plot combines a *P*-value statistical test with the fold-regulation change-enabling identification of genes with both large and small expression changes that are statistically significant. (C) A volcano plot of 48-hour E_4 treatment. (D) Effects of E_2 and E_4 alone after 7 days of treatment. (E) Flow cytometry of 72-hour E_2 and E_4 treatments. (B and C) Green represents downregulated, black unchanged, and red upregulated. Data are mean ± S.D. from three independent experiments performed in triplicate analyzed by one-way ANOVA. Veh, vehicle.

Supplemental Fig. 5C). Interestingly, there was a 9.46-fold ($P < 0.05$) downregulation of EIF2AK3 (PERK) (Supplemental Fig. 5C), which might play a role in MCF-7:5C cells' delayed course of apoptosis with BMI-135 treatment compared with E_2 and E_4. After a 72-hour treatment with 1 μM BMI-135, there was an intensified (or terminal) UPR gene regulation compared with 48 hours, with an upregulation of CEBPB ($P < 0.001$), INHBE ($P < 0.001$), PPP1R15A (GADD34, $P < 0.001$), DDIT3 (CHOP, $P < 0.001$), and ERN1 (IRE1α, $P < 0.001$). This is coupled with a downregulation of the ERAD genes, HTRA4 ($P < 0.001$), SEL1L ($P < 0.01$), and HERPUD1 ($P < 0.001$); the chaperone gene HSPA2 ($P < 0.001$); and the lipid metabolism gene MBTPS1 ($P < 0.001$) (Fig. 8B; Supplemental Fig. 5D).

The heat map of MCF-7:5C cells with BMI-135 treatment at 72 hours (Fig. 8A) displays a general UPR gene downregulation (situated on the right side of the heat map) compared with vehicle control (situated on the left). This general downregulation by 72 hours (Fig. 8B; Supplemental Fig. 5D) highlights MCF-7:5C cells' trajectory to undergo apoptosis by 96 hours (Fig. 8E).

Cell viability and proliferation assays showed a decline in MCF-7:5C cell DNA amount with BPTPE treatment by day 8 (Supplemental Fig. 4D). Furthermore, flow cytometry showed apoptosis by day 8 (annexin staining 31.5% with BPTPE vs. vehicle control 9.4%) (Supplemental Fig. 4E). The time point of day 7 was chosen to investigate the proapoptotic UPR gene regulation, which precedes apoptosis by day 8. Another time point of day 3 was chosen to compare and contrast the UPR gene regulation with that of day 7 and show how this regulation is dynamic and culminates over time.

After a 3-day treatment with 1 μM BPTPE, there was a relatively minor UPR gene activation compared with the one seen by day 7 (Supplemental Figs. 4, B and C and 5, E and F). Interestingly, there was a 2.15-fold ($P < 0.001$) downregulation of EIF2AK3 with 3-day BPTPE treatment (Supplemental Fig. 5E), which might play a role in MCF-7:5C cells' delayed course of apoptosis with BPTPE treatment compared with E_2 and E_4. This is also observed with BMI-135's early treatment time point (Supplemental Fig. 5C). After a 7-day treatment with BPTPE, there was a downregulation of the ERAD gene HERPUD1 ($P < 0.001$), the lipid metabolism genes INSIG2 ($P < 0.001$) and MBTPS1 ($P < 0.001$), and the chaperone genes HSPA2 ($P < 0.001$) and DNAJB9 ($P < 0.001$) (Supplemental Figs. 4B and 5F).

The heat map of MCF-7:5C cells with BPTPE treatment at day 7 (Supplemental Fig. 4A) displays a general UPR gene downregulation (situated on the left side of the heat map) compared with vehicle control (situated on the right). This general downregulation by day 7 (Supplemental Figs. 4B and 5F) highlights MCF-7:5C cells' programming to undergo apoptosis by day 8 (Supplemental Fig. 4E).

The statistically significant regulated UPR genes with test compounds are stated and grouped at select time points (Fig. 9) to show the similar terminal UPR regulation preceding apoptosis.

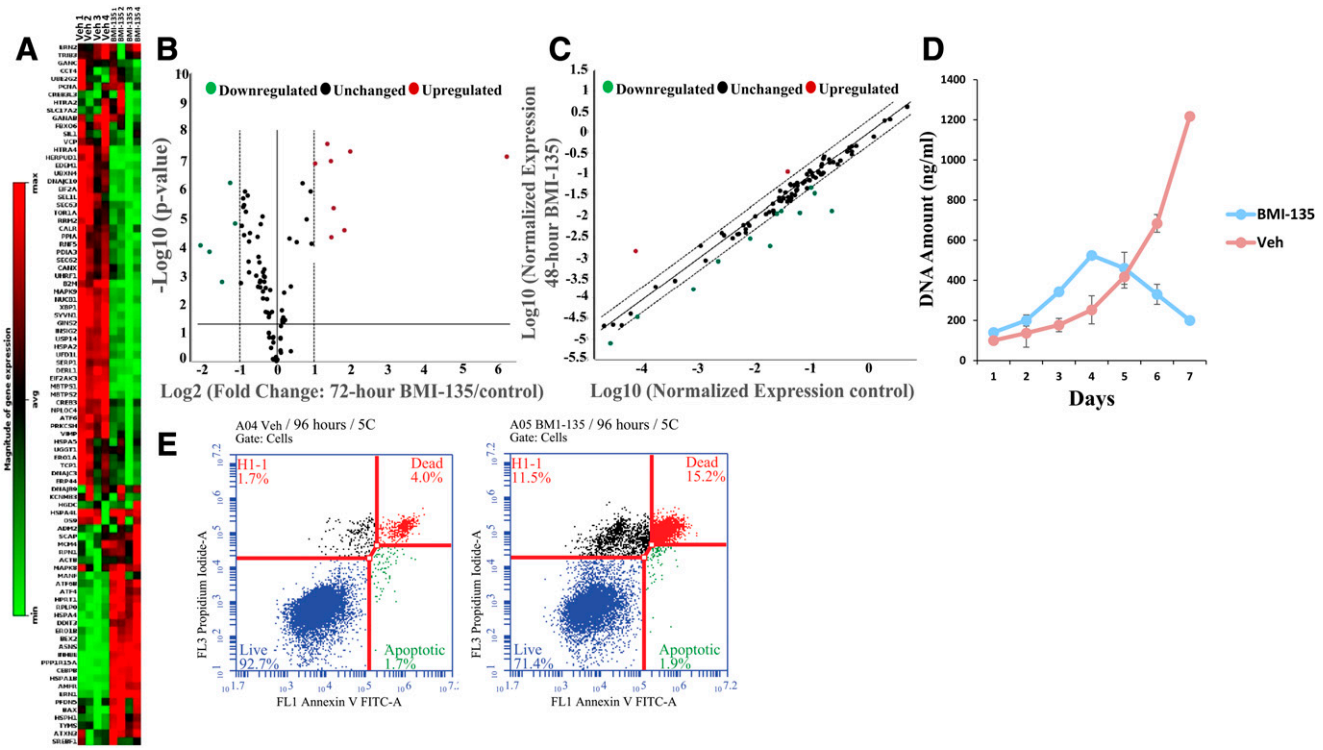

Fig. 8. Human UPR RT^2 PCR profiler PCR arrays, proliferation assays, and annexin V staining in MCF-7:5C cells with 48-hour, 72-hour, 96-hour, and 7-day BMI-135 treatments. (A) A heat map of 72-hour BMI-135 treatment, providing a visualization of the fold changes in expression between the select groups (from left to right; vehicle and BMI-135, respectively) for every gene in the array in the context of the array layout. (B) A volcano plot of 72-hour BMI-135 treatment. (C) A scatter plot of 48-hour BMI-135 treatment comparing the normalized expression of every gene on the array between the two select groups by plotting them against one another to quickly visualize large gene-expression changes. The central line indicates unchanged gene expression. The dotted lines indicate the selected fold-regulation threshold. Data points beyond the dotted lines in the upper left and lower right sections meet the selected fold-regulation threshold. (D) Effects of BMI-135 alone after 7 days of treatment. (E) Flow cytometry of 96-hour BMI-135 treatment. (B and C) Green represents downregulated, black unchanged, and red upregulated. Data are mean ± S.D. from three independent experiments performed in triplicate analyzed by one-way ANOVA. Veh, vehicle.

E_4 and BMI-135 Induce ThT Fluorescence as a Marker of UPR. ThT has been successfully used for the detection and quantification of EnR stress and the UPR in living cells (Beriault and Werstuck, 2013) given that it directly interacts with the accumulated misfolded protein amyloid during the UPR (Beriault and Werstuck, 2013).

The "blue" Hoechst 33342 dye was used for counter-staining as a live cell nuclear dye (channel A), the "green" ThT dye was used as a UPR-indicative dye (channel B), and a colocalization of ThT and Hoechst 33342 dyes is shown (channel C). 17β-Estradiol and E_4 were shown to induce ThT fluorescence by 48 hours, like the induction seen with positive control thapsigargin, and compared with vehicle control (Supplemental Fig. 6B). After 48-hour treatment, E_4 had the highest ThT relative intensity/cell of 1.244892, and this was followed by thapsigargin of 0.875072; E_2 of 0.741126; and BMI-135 of 0.497225, compared with vehicle control of 0.27594 (Table 2A).

BMI-135 induced a stronger delayed ThT fluorescence by 72 hours (Fig. 10B; Table 2B) compared with that seen by 48 hours (Supplemental Fig. 6B; Table 2A). The relative intensity/cell with 48-hour BMI-135 treatment was 0.497225 compared with vehicle control 0.27594 (Table 2A). However, the relative intensity/cell with 72-hour BMI-135 treatment was 4.878173 compared with vehicle control of 0.29573 (Table 2B). The relative intensity/cell over time is represented in Table 2.

E_4 and BMI-135 Induce Apoptosis in Multiple Endocrine-Resistant and Estrogen-Independent BC Models. Flow cytometry was used to determine whether the type of stress-induced cell death in MCF-7:5C, MCF-7:2A, and MCF-7:RAL cells was apoptosis when treated with 1 μM E_4 and 1 μM BMI-135.

In MCF-7:5C, 1 μM E_4 induced apoptosis (annexin staining 12.6% vs. vehicle control 4.5%) similar to the time course of 1 nM E_2 (annexin staining 14.8% vs. vehicle control 4.5%) (Fig. 7E), which was by 72 hours. However, MCF-7:5C's apoptosis with BMI-135 treatment (annexin staining 17.1% vs. vehicle control 5.7%) was delayed by 96 hours (Fig. 8E representing 96 hours; Supplemental Fig. 8D representing 72 hours). The antagonist 4OHT (as a negative control) and its pairing with E_2, E_4, and BMI-135 did not induce apoptosis by 72 or 96 hours, as predicted (unpublished data).

In MCF-7:2A, E_4 induced apoptosis (annexin staining 6.7% vs. vehicle control 0.8%) similar to the time course of E_2 (annexin staining 8% vs. vehicle control 0.8%) (Supplemental Fig. 8A), which was by day 9. However, MCF-7:2A's apoptosis with BMI-135 treatment (annexin staining 7.3% vs. vehicle control 2.2%) was delayed by day 13 (Supplemental Fig. 8B representing day 13; Supplemental Fig. 8C representing day 9). The antagonist 4OHT (as a negative control) and its pairing with E_2, E_4, and BMI-135 did not induce apoptosis by day 9 or 13, as predicted (unpublished data).

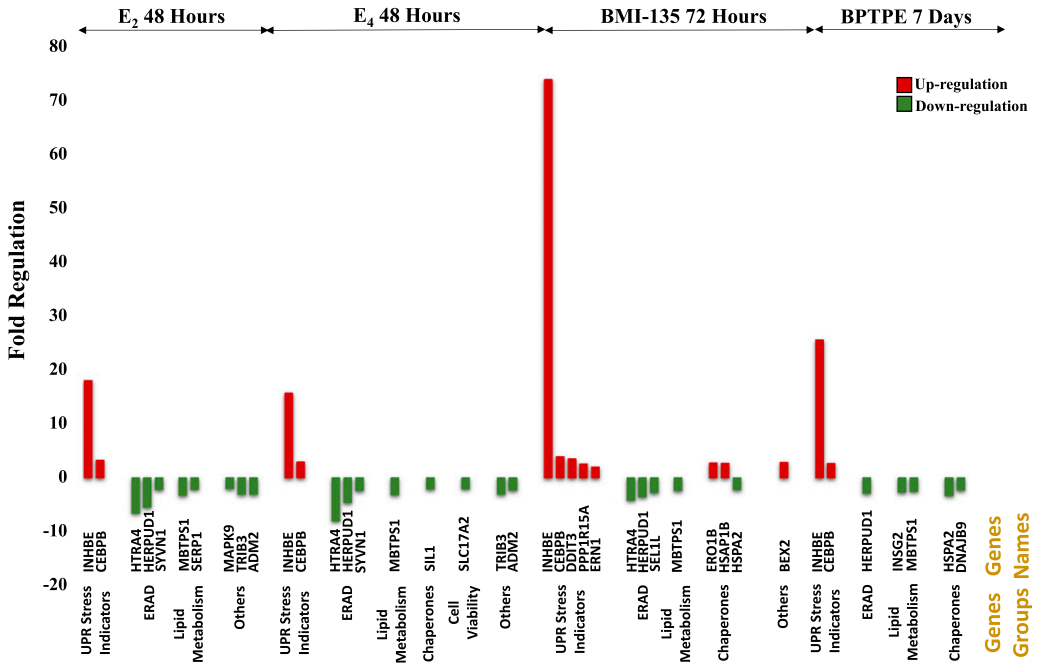

Fig. 9. A schematic representation of the statistically significant UPR genes and their gene groupings with test compounds. The *y*-axis displays fold regulation, and the *x*-axis states the UPR genes and their groupings, demonstrating a signature proapoptotic UPR regulation at different time points with test compounds. Green represents downregulation and red upregulation. The ERAD proteins decrease cellular stress by degrading severely misfolded or unfolded proteins, and chaperones do so by folding the misfolded or unfolded proteins that could be rescued (Hetz, 2012). Lipid metabolism-related proteins play a critical role in lipid metabolism and homeostasis to combat cellular stress (Hetz and Saxena, 2017). The downregulation of these UPR gene groups ($P < 0.05$) as well as the upregulation of UPR stress indicators (INHBE and CEBPB) ($P < 0.05$) form a UPR phase whose regulation is characterized as terminal/proapoptotic (Maly and Papa, 2014; Grootjans et al., 2016).

In MCF-7:RAL, E_4 induced apoptosis (annexin staining 7.6% vs. vehicle control 5.3%) similar to the time course of E_2 (annexin staining 9% vs. control 5.3%) (Supplemental Fig. 9A), which was by day 14. However, MCF-7:RAL's apoptosis with BMI-135 (annexin staining 8% vs. control 0.8%) was delayed until day 17 (Supplemental Fig. 9B representing day 17; Supplemental Fig. 9C representing day 14). The antagonists 4OHT and raloxifene and their pairing with E_2, E_4, and BMI-135 did not induce apoptosis by day 14 or 17, as predicted (Supplemental Fig. 9A). Interestingly, treatment of MCF-7:RAL cells with ICI for 3 weeks caused a decline in cell DNA amount ($P < 0.05$) (Supplemental Fig. 2C); however, this was not due to apoptosis (Supplemental Fig. 9D). Such observed effect of ICI in MCF-7:RAL could be attributed to growth inhibition by preventing cell replication.

Inhibition of PERK Pathway Blocks Apoptosis in MCF-7:5C with E_4 and BMI-135 Treatments. Blocking the UPR transducer PERK with 10 μM GSK G797800 in combination with 1 nM E_2 and in combination with 1 μM E_4 by 72 hours inhibited apoptosis (annexin staining 7.8% and 7.9%, respectively, vs. vehicle control 7%) (Supplemental Fig. 7A) compared with E_2- and E_4-alone treatments that trigger apoptosis (Fig. 7E) and compared with the negative control GSK G797800–alone treatment that does not trigger apoptosis (annexin staining 5.7% vs. vehicle control 7%) (Supplemental Fig. 7A).

Blocking PERK with 10 μM GSK G797800 in combination with 1 μM BMI-135 by 96 hours inhibited apoptosis (annexin staining 4% vs. vehicle control 5.7%) (Fig. 11A) compared with BMI-135–alone treatment that triggers apoptosis (Fig. 11A) and compared with GSK G797800–alone treatment (annexin staining 5.5% vs. control 5.7%) (Fig. 11A).

Inhibition of IRE1α:XBP1s Pathway Enhances Apoptosis in MCF-7:5C with E_4 and BMI-135 Treatments. The compound MKC-3946 inhibits IRE1α by inhibiting basal XBP1 splicing. Blocking the UPR transducer IRE1α with 20 μM MKC-3946 in combination with 1 μM E_4 by 72 hours induces more apoptosis (annexin staining 34.1% vs. control 1.4%) (Supplemental Fig. 7B) compared with E_4-alone treatment that triggers apoptosis (annexin staining 18.6% vs. control 1.4%) (Supplemental Fig. 7B) and compared with MKC-3946–alone treatment that triggers apoptosis (annexin staining 8.8% vs. control 1.4%) (Supplemental Fig. 7B).

Blocking IRE1α with 20 μM MKC-3946 in combination with 1 μM BMI-135 by 96 hours induces more apoptosis (annexin staining 33.3% vs. control 1.4%) (Fig. 11B) compared with BMI-135–alone treatment (annexin staining 26.5% vs. control 1.4%) (Fig. 11B) and compared with MKC-3946–alone treatment (annexin staining 8.8% vs. control 1.4%) (Fig. 11B).

Discussion

Estetrol is a naturally occurring fetal estrogen, which is associated with a low risk of drug-drug interactions (CYP450 family) and a neutral impact on risk markers of venous thromboembolism (Singer et al., 2014; Coelingh Bennink et al., 2017; Verhoeven et al., 2018). BMI-135 is a member of a new class of estrogen mimics, which did not cause significant uterine proliferation (Molloy et al., 2014; Xiong et al., 2016). Estetrol and the ShERPA TTC-352 are currently being evaluated in endocrine-resistant MBC clinical trials (O'Regan et al., 2019;

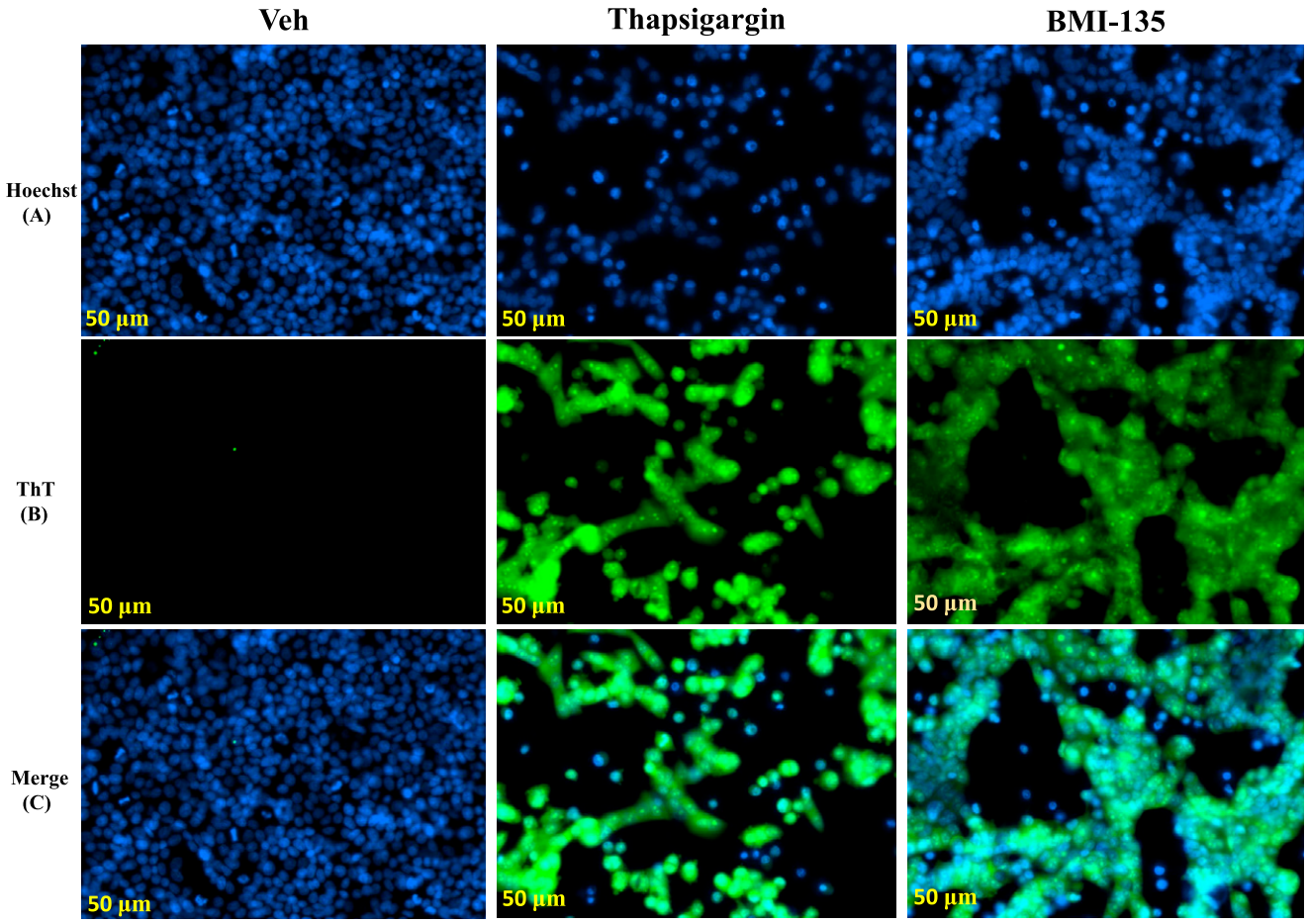

Fig. 10. Detection of UPR in live MCF-7:5C cells using ThT fluorescent dye after 72-hour treatments as measured by the ZEISS Celldiscoverer 7 microscope. (A) Hoechst 33342 dye single panel (blue). (B) ThT dye single panel (green). (C) A merge or colocalization ThT + Hoechst 33342 dyes panel (blue and green). Treatments included 0.1% DMSO (vehicle control), 1 μM thapsigargin (positive control; promoting EnR stress by disrupting EnR Ca^{2+} homeostasis), and 1 μM BMI-135. Scale bar, 50 μM. ThT relative intensity/cell, per treatment, is the mean of three biologic repeats with S.D. (Table 2B). Veh, vehicle.

Schmidt et al., 2020). Our study, in a wide range of endocrine-resistant and estrogen-independent BC cell models as well as an endometrial cancer cell model, shows E_4 and BMI-135 to be less potent full estrogen agonists (Figs. 2–5 and 6, B and F) with the induction of terminal UPR and apoptosis as their antitumor mechanism of action (Figs. 7–12; Supplemental Figs. 5, B and D and 6–9). Although BMI-135 exhibits a slightly delayed UPR-and-apoptosis biology compared with E_2 and E_4 (Figs. 7–11; Supplemental Figs. 6–9), it is still distinct from the much delayed UPR-and-apoptosis biology of the benchmark partial agonist BPTPE (Supplemental Fig. 4).

The application of long-term adjuvant endocrine therapy (Jordan et al., 1979) to treat ER-positive BC is invaluable for patient care. As a result, women's lives are extended or saved (Early Breast Cancer Trialists' Collaborative Group, 1998; Goss et al., 2003, 2005). Nonetheless, recurrence of endocrine-resistant stage IV BC is common (Pisani et al., 2002), hence the discovery of new therapeutic options remains a clinical priority.

Cell models (Pink et al., 1995; Liu et al., 2003; Lewis et al., 2005b; Ariazi et al., 2011; Fan et al., 2014) and athymic mice models (Gottardis and Jordan, 1988; Gottardis et al., 1989a,b; Yao et al., 2000) deciphered the evolution of acquired TAM resistance over years to eventually give rise to a vulnerability in BC: E_2-induced apoptosis (Jordan, 2008; Jordan, 2015). Although estrogen is approved to treat BC, there is a reluctance to use estradiol as a salvage therapy in stage IV BC because of AEs. As a result, safer estrogenic alternatives are being considered.

Our goal was to compare and contrast the actions of E_4 and BMI-135 with the well characterized partial agonist BPTPE. Our earlier pharmacological studies classified ER-binding ligands into agonists, partial agonists, and antagonists (Jordan, 1984; Jordan et al., 1984, 1986; Murphy et al., 1990a) and are essential to decipher the current molecular mechanisms of E_2-induced apoptosis through the ER signal transduction pathway. These functional cell-based assays (Lieberman et al., 1983a,b; Jordan and Lieberman, 1984; Jordan et al., 1986) dovetailed with the subsequent X-ray crystallography studies of the agonist and antagonist ER complexes of the LBD (Brzozowski et al., 1997; Shiau et al., 1998). Our earlier biologic studies described E_2-induced apoptosis (Jordan, 2015). Our current study shows that E_4 and BMI-135:ERα complexes initiate and modulate the UPR (Figs. 7–12; Supplemental Figs. 5–7). This is an ERα-mediated (Supplemental Fig. 2) activation of the unfolded proteins' synthesis and thus of cellular stress.

The intrinsic activity of the ER complex was evaluated by comparing and contrasting TFF1 and GREB1 estrogen-regulated gene activation with E_2, BMI-135, BPTPE, and endoxifen

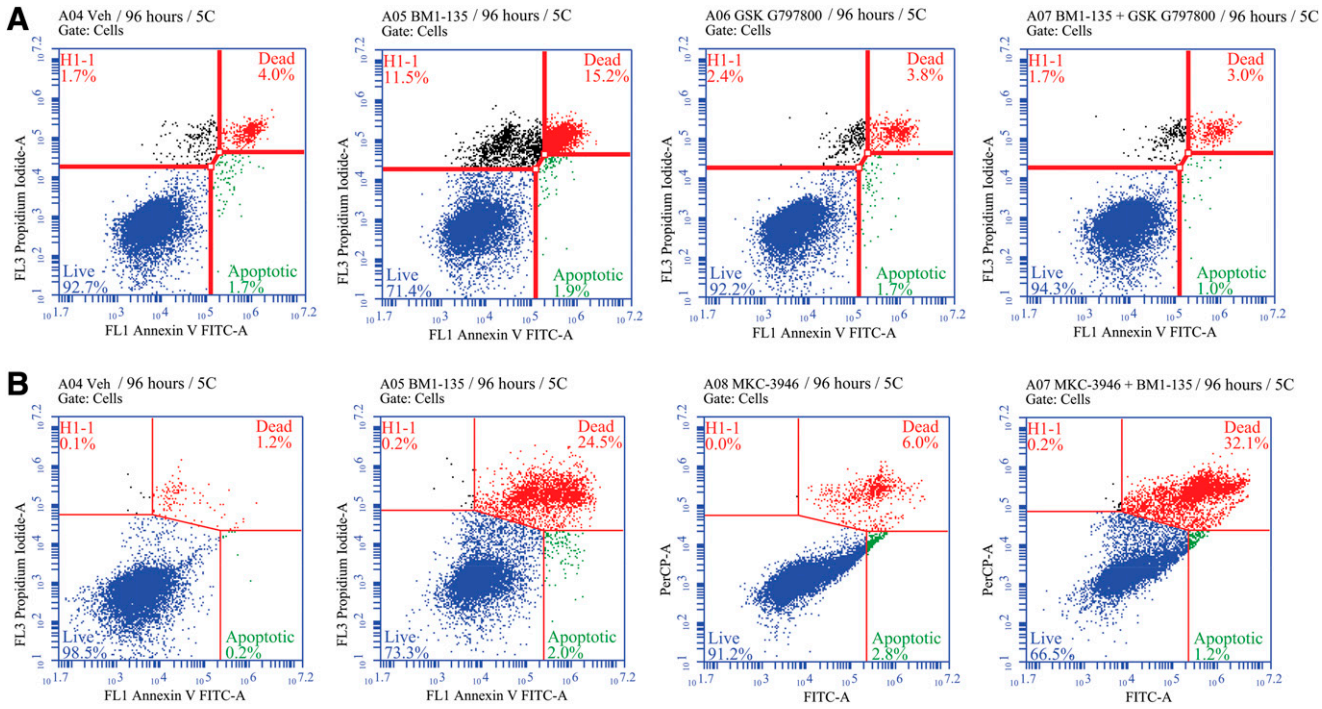

Fig. 11. Flow cytometry in MCF-7:5C cells with BMI-135 plus a PERK inhibitor or an IRE1α inhibitor after 96-hour treatments. (A) MCF-7:5C cells were treated with 0.1% DMSO (vehicle control), 1 μM BMI-135, 10 μM GSK G797800, and 1 μM BMI-135 + 10 μM GSK G797800 then stained with annexin V–FITC and propidium iodide and analyzed by flow cytometry. Viable cells (left lower quadrant) are annexin V–FITC− and PI−; early apoptotic cells (right lower quadrant) are annexin V–FITC+ and PI−; dead cells (left upper quadrant) are PI+, and late apoptotic cells (right upper quadrant) are annexin V–FITC+ and PI+. An increased, late apoptotic effect is observed in the right upper quadrant. (B) MCF-7:5C cells were treated with 0.1% DMSO (vehicle control), 1 μM BMI-135, 20 μM MKC-3946, and 1 μM BMI-135 + 20 μM MKC-3946. Data are mean ± S.D. from three independent experiments analyzed by one-way ANOVA. (A and B).

treatments in WT MCF-7 and LTED MCF-7:5C cells (Fig. 3). The pharmacology of each ligand as a full agonist (E_2, E_4, and BMI-135) or a partial agonist (BPTPE) or an antagonist with no intrinsic activity (endoxifen) mirrored the pharmacology in cells (Fig. 2).

Molecular modeling studies demonstrated that E_4, BMI-135, and BPTPE bind to the classic agonist conformation of ERα, similar to E_2 (Fig. 6, A, C, and E). The flexible docking and MD simulations performed for BMI-135:ERα complex show the dynamic profile of the system to be similar to E_2 (Supplemental Fig. 3A) with the ligand firmly bound to the active site (Supplemental Fig. 3B). Although BMI-135 is larger than E_2, the same contacts have been observed, with the notable exception of the H-bond to His524 (Fig. 6B). These H-bonds and hydrophobic contacts are stable for both ligands, with slightly larger frequencies of occurrence with E_2 (Supplemental Fig. 11, A and B), which indicates a stronger binding mode of E_2. BPTPE exhibits equivalent binding contacts to E_2 (Fig. 6, C and D) but forms a distinctive robust H-bond with Thr347 (Supplemental Fig. 11C), which induces the stability of the ligand binding but increases the mobility of H12 and the loop connecting H11 and H12, which affects the overall stability of the system. This is most likely responsible for the partial agonist profile of BPTPE. These data support the molecular classification of E_4 and BMI-135 as full agonists and further explain their observed biologic behavior.

A comparison of E_4, BMI-135, and BPTPE in multiple WT and LTED BC cell lines (Fig. 2; Supplemental Fig. 1) demonstrates the partial agonist actions of BPTPE on both growth (Figs. 2, A–E and 3, A and B; Supplemental Fig. 1, A–C and F) and E_2-induced apoptosis (Figs. 2, F–H and 3, C and D; Supplemental Fig. 4, D and E). All experiments used BPTPE as a well characterized partial agonist (Jordan and Lieberman, 1984), which triggers delayed E_2-induced apoptosis in LTED BC cells compared with E_2 (Obiorah et al., 2014; Obiorah and Jordan, 2014) (Supplemental Fig. 4E). The mechanism is shown here to be through a delay in the induction of the proapoptotic UPR signaling (Supplemental Figs. 4, B and C and 5, E and F).

Delayed apoptosis with BPTPE (which contains a free para-hydroxyl on the phenyl ring) mirrors the delayed apoptosis with the synthesized angular triphenylethylene (TPE) derivative 3OH**TPE** (which contains the free para-hydroxyl) (Maximov et al., 2020). The other synthesized TPE derivative Z2OH**TPE** does not contain the free para-hydroxyl and causes early apoptosis, similar to E_2 (Maximov et al., 2020). This free para-hydroxyl in BPTPE and 3OHTPE is part of the anti-estrogenic side chain of endoxifen, which prevents the complete closure of ERα's H12 over the ligand:LBD (Supplemental Fig. 11C). This delays the coactivators' recruitment to the ER to form a transcriptionally active complex (Fig. 5B), which delays the ligand:ERα–induced transcription and translation of the unfolded proteins, resulting in delayed apoptosis (Supplemental Fig. 4).

Although BMI-135 does not exhibit the pharmacology of BPTPE (Figs. 2–5 and 6, A and B; Table 1), there is still a slight delay in the induction of the terminal UPR signaling and apoptosis, which is mediated by the BMI-135:ERα complex (Figs. 8, B and E and 10B; Supplemental Fig. 5D;

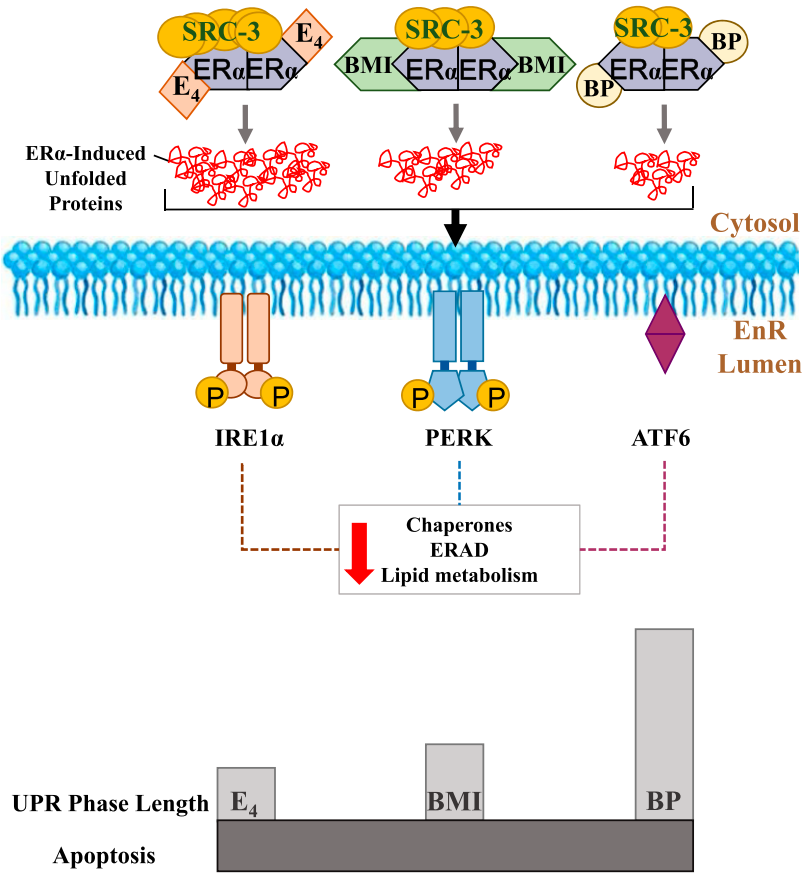

Fig. 12. Schematic representation of the study's concluded antitumor molecular mechanisms of E_4, BMI-135, and BPTPE in LTED endocrine-resistant BC MCF-7:5C. Estetrol:ERα complex recruits the most coactivator SRC-3 and thus induces the most accumulation of unfolded proteins (highest threshold of stress), followed by BMI-135:ERα (BMI-135 is referred to as BMI in the illustration) and BPTPE:ERα (BPTPE is referred to as BP in the illustration). This differential ligand:ERα:coactivator-induced endoplasmic reticulum stress activates the transducers of the UPR, with a downregulation of chaperons, ERAD, and lipid metabolism genes and proteins ($P < 0.05$), which are considered prosurvival mechanisms. This downregulation state constitutes the proapoptotic UPR phase, which is reached quickly with E_4, followed by BMI-135 and BPTPE, and eventually induces apoptosis.

Table 2B for the 72-hour time point vs. Fig. 8C; Supplemental Figs. 5C, 6B, and 8D; Table 2A for the 48-hour time point).

The ChIP assay (Fig. 5) is valuable in understanding the delayed apoptotic biology with BMI-135 and BPTPE. Earlier studies (Sengupta et al., 2013; Obiorah et al., 2014) demonstrated a reduction in the binding of the BPTPE:ERα:SRC-3 complex using the ChIP assay in MCF-7 cells, which is reproduced here (Fig. 5, A and B). A reduced DNA binding of the partial agonist complex occurs, which correlates with a reduction in the efficacy of the complex to synthesize misfolded or unfolded proteins, hence with a delay in the induction of the terminal UPR and apoptosis compared with E_2 (Supplemental Fig. 4). Although BMI-135 recruits equivalent quantities of ERα (Fig. 5A), there is a reduced recruitment of the coactivator SRC-3 compared with E_2 and E_4. Nonetheless, BMI-135:ERα's recruitment of SRC-3 is higher than that with BPTPE ($P < 0.05$) (Fig. 5B). This correlates with BMI-135's slightly delayed induction of the terminal UPR and apoptosis (Fig. 8).

The downregulation of the prosurvival mechanisms, chaperones, ERAD, and lipid metabolism genes ($P < 0.05$), alongside the upregulation of marker UPR stress proteins (INHBE and CEBPB) ($P < 0.05$) constitute the terminal/proapoptotic UPR phase and underscore the antitumor mechanism of E_2, E_4, BMI-135, and BPTPE (Figs. 7–9 and 12; Supplemental Figs. 4 and 5).

Apoptosis with E_4 and BMI-135 treatments was prevented by blocking the PERK pathway (Fig. 11A; Supplemental Fig. 7A). By contrast, blocking the IRE1α:XBP1s pathway after E_4 and BMI-135 treatments enhanced apoptosis (Fig. 11B; Supplemental Fig. 7B). These data demonstrate the modulation of apoptosis with E_4 and BMI-135 through the modulation of UPR's subcellular sensors.

The timing of UPR-indicative ThT fluorescence with E_4 and BMI-135 is synchronic with that of their proapoptotic UPR gene regulation ($P < 0.05$). The ThT fluorescence and terminal UPR gene regulation were shown to be by 48 hours with E_2 and E_4 (before apoptosis by 72 hours), by 72 hours with BMI-135 (before apoptosis by 96 hours), and by day 7 with BPTPE (before apoptosis by day 8) (Figs. 7, 8, and 10B; Supplemental Figs. 4, 5, and 6B; Table 2).

Translational research (Gottardis et al., 1988) identified a potential link between TAM treatment and the occurrence of endometrial cancer in patients (Jordan and Assikis, 1995). Raloxifene does not have an increased risk of endometrial cancer in clinical trials (Cummings et al., 1999; Vogel et al., 2006). BMI-135 is a raloxifene derivative (Fig. 1) (Xiong et al., 2016) and was tested to determine whether the ShERPA BMI-135:ER:coregulators complex is an agonist in the human endometrial cancer cell line Ishikawa transfected with 5x-ERE (Fig. 4). BPTPE exhibited a partial agonist activity (Fig. 4A), but both E_4 and BMI-135 exhibited a less potent full agonist activity compared with E_2 (Fig. 4A). This effect is mediated via the Ishikawa ERα (Fig. 4B). Although BMI-135 was shown not to induce uterine growth in a mouse xenograft model (Xiong et al., 2016), based on this study's observations, it would be wise to require an endometrial screening for patients with BC receiving E_4 or BMI-135.

Raloxifene induces acquired resistance as evidenced by SERM-stimulated BC cell growth (Liu et al., 2003; Balaburski et al., 2010) (Fig. 2H; Supplemental Figs. 1F and 2C). Such

laboratory data have clinical significance because a case report of an antiestrogen withdrawal effect with raloxifene was reported (Lemmo, 2016). Raloxifene-resistant BC-stimulated growth has not been widely reported during the decades of treatment in patients with osteoporosis. This is surprising, but perhaps clinicians have not been aware of this form of SERM resistance. Nevertheless, our findings here (Supplemental Fig. 9, A and B) suggest that E_4 or an ShERPA could be deployed after raloxifene discontinuation to induce tumor regression through apoptosis in raloxifene-resistant BC. Furthermore, ICI could be deployed, as we have shown here that it has a growth inhibitory effect (Supplemental Figs. 1F, 2C, and 9D).

Estrogen receptor-positive BC constitutes more than 70% of all BCs (Clark et al., 1984). Rosenberg and coworkers (2015) projected BC cases in the United States to double by 2030 compared with cases in 2011. The majority will be ER-positive BC. The development of new agents to treat ER-positive endocrine-resistant MBC remains a priority. Overall, the results of our work support the continuation of future clinical trials with the new agents E_4 and ShERPAs.

Acknowledgments

We thank Dr. Sean W. Fanning and Dr. Geoffrey L. Greene and the Ben May Department for Cancer Research for providing the X-ray crystallography of TTC-352:ERα. B.A. holds a dual position, acting as the Dallas/Fort Worth Living Legend Fellow of Cancer Research at the Department of Breast Medical Oncology, the University of Texas Anderson Cancer Center (TX), and a split-site PhD trainee under model C "Applicants of Very High Quality" at the Faculty of Biological Sciences, the University of Leeds (West Yorkshire, UK).

Authorship Contributions

Participated in research design: Abderrahman, Jordan.

Conducted experiments: Abderrahman, Maximov, Hanspal, Fan.

Contributed new reagents or analytic tools: Curpan, Xiong, Tonetti, Thatcher.

Performed data analysis: Abderrahman, Curpan, Jordan.

Wrote or contributed to the writing of the manuscript: Abderrahman, Maximov, Curpan, Tonetti, Thatcher, Jordan.

References

Abderrahman B and Jordan VC (2016) The modulation of estrogen-induced apoptosis as an interpretation of the women's health initiative trials. *Expert Rev Endocrinol Metab* **11**:81–86.

Abot A, Fontaine C, Buscato M, Solinhac R, Flouriot G, Fabre A, Drougard A, Rajan S, Laine M, Milon A, et al. (2014) The uterine and vascular actions of estetrol delineate a distinctive profile of estrogen receptor α modulation, uncoupling nuclear and membrane activation. *EMBO Mol Med* **6**:1328–1346.

Anderson GL, Limacher M, Assaf AR, Bassford T, Beresford SA, Black H, Bonds D, Brunner R, Brzyski R, Caan B, et al.; Women's Health Initiative Steering Committee (2004) Effects of conjugated equine estrogen in postmenopausal women with hysterectomy: the Women's Health Initiative randomized controlled trial. *JAMA* **291**:1701–1712.

Ariazi EA, Cunliffe HE, Lewis-Wambi JS, Slifker MJ, Willis AL, Ramos P, Tapia C, Kim HR, Yerrum S, Sharma CG, et al. (2011) Estrogen induces apoptosis in estrogen deprivation-resistant breast cancer through stress responses as identified by global gene expression across time. *Proc Natl Acad Sci USA* **108**:18879–18886.

Balaburski GM, Dardes RC, Johnson M, Haddad B, Zhu F, Ross EA, Sengupta S, Klein-Szanto A, Liu H, Lee ES, et al. (2010) Raloxifene-stimulated experimental breast cancer with the paradoxical actions of estrogen to promote or prevent tumor growth: a unifying concept in anti-hormone resistance. *Int J Oncol* **37**:387–398.

Beriault DR and Werstuck GH (2013) Detection and quantification of endoplasmic reticulum stress in living cells using the fluorescent compound, Thioflavin T. *Biochim Biophys Acta* **1833**:2293–2301.

Brzozowski AM, Pike AC, Dauter Z, Hubbard RE, Bonn T, Engström O, Ohman L, Greene GL, Gustafsson JA, and Carlquist M (1997) Molecular basis of agonism and antagonism in the oestrogen receptor. *Nature* **389**:753–758.

Chalasani P, Stopeck A, Clarke K, and Livingston R (2014) A pilot study of estradiol followed by exemestane for reversing endocrine resistance in postmenopausal women with hormone receptor-positive metastatic breast cancer. *Oncologist* **19**: 1127–1128.

Chlebowski Rowan T, Anderson Garnet L, Aragaki Aaron K, Manson JoAnn E, Stefanick Marcia L, Pan Kathy, Barrington Wendy, Kuller Lewis H, Simon Michael S, Lane Dorothy, et al. (2020) Association of Menopausal Hormone Therapy With Breast Cancer Incidence and Mortality During Long-term Follow-up of the Women's Health Initiative Randomized Clinical Trials. *JAMA* **324**:369–380.

Clark GM, Osborne CK, and McGuire WL (1984) Correlations between estrogen receptor, progesterone receptor, and patient characteristics in human breast cancer. *J Clin Oncol* **2**:1102–1109.

Coelingh Bennink HJ, Verhoeven C, Dutman AE, and Thijssen J (2017) The use of high-dose estrogens for the treatment of breast cancer. *Maturitas* **95**:11–23.

Coelingh Bennink HJ, Verhoeven C, Zimmerman Y, Visser M, Foidart JM, and Gemzell-Danielsson K (2016) Clinical effects of the fetal estrogen estetrol in a multiple-rising-dose study in postmenopausal women. *Maturitas* **91**: 93–100.

Cole MP, Jones CT, and Todd ID (1971) A new anti-oestrogenic agent in late breast cancer. An early clinical appraisal of ICI46474. *Br J Cancer* **25**:270–275.

Creinin MD, Rosing J, Jost M, Kinet V, Chatel G, and Foidart JM (2019) Estetrol combined with drospirenone: a new oral contraceptive with a favorable hemostatic profile. *Obstet Gynecol* **133**:7S.

Cummings SR, Eckert S, Krueger KA, Grady D, Powles TJ, Cauley JA, Norton L, Nickelsen T, Bjarnason NH, Morrow M, et al. (1999) The effect of raloxifene on risk of breast cancer in postmenopausal women: results from the MORE randomized trial. Multiple Outcomes of Raloxifene Evaluation. *JAMA* **281**:2189–2197.

Dutman E, Zimmerman Y, and Coelingh-Bennink H (2017) The effects of the human fetal estrogen estetrol (E4) in healthy men to estimate its potential use for the treatment of prostate cancer. *Eur Urol Suppl* **16**:e362–e364.

Early Breast Cancer Trialists' Collaborative Group (1998) Tamoxifen for early breast cancer: an overview of the randomised trials. *Lancet* **351**:1451–1467.

Ellis MJ, Gao F, Dehdashti F, Jeffe DB, Marcom PK, Carey LA, Dickler MN, Silverman P, Fleming GF, Kommareddy A, et al. (2009) Lower-dose vs high-dose oral estradiol therapy of hormone receptor-positive, aromatase inhibitor-resistant advanced breast cancer: a phase 2 randomized study. *JAMA* **302**:774–780.

Engel LW, Young NA, Tralka TS, Lippman ME, O'Brien SJ, and Joyce MJ (1978) Establishment and characterization of three new continuous cell lines derived from human breast carcinomas. *Cancer Res* **38**:3352–3364.

Fan P, Agboke FA, Cunliffe HE, Ramos P, and Jordan VC (2014) A molecular model for the mechanism of acquired tamoxifen resistance in breast cancer. *Eur J Cancer* **50**:2866–2876.

Fan P, Griffith OL, Agboke FA, Anur P, Zou X, McDaniel RE, Creswell K, Kim SH, Katzenellenbogen JA, Gray JW, et al. (2013) c-Src modulates estrogen-induced stress and apoptosis in estrogen-deprived breast cancer cells. *Cancer Res* **73**: 4510–4520.

Gérard C, Mestdagt M, Tskitishvili E, Communal L, Gompel A, Silva E, Arnal JF, Lenfant F, Noel A, Foidart JM, et al. (2015) Combined estrogenic and antiestrogenic properties of estetrol on breast cancer may provide a safe therapeutic window for the treatment of menopausal symptoms. *Oncotarget* **6**:17621–17636.

Goss PE, Ingle JN, Martino S, Robert NJ, Muss HB, Piccart MJ, Castiglione M, Tu D, Shepherd LE, Pritchard KI, et al. (2003) A randomized trial of letrozole in postmenopausal women after five years of tamoxifen therapy for early-stage breast cancer. *N Engl J Med* **349**:1793–1802.

Goss PE, Ingle JN, Martino S, Robert NJ, Muss HB, Piccart MJ, Castiglione M, Tu D, Shepherd LE, Pritchard KI, et al. (2005) Randomized trial of letrozole following tamoxifen as extended adjuvant therapy in receptor-positive breast cancer: updated findings from NCIC CTG MA.17. *J Natl Cancer Inst* **97**:1262–1271.

Gottardis MM, Jiang SY, Jeng MH, and Jordan VC (1989a) Inhibition of tamoxifen-stimulated growth of an MCF-7 tumor variant in athymic mice by novel steroidal antiestrogens. *Cancer Res* **49**:4090–4093.

Gottardis MM and Jordan VC (1988) Development of tamoxifen-stimulated growth of MCF-7 tumors in athymic mice after long-term antiestrogen administration. *Cancer Res* **48**:5183–5187.

Gottardis MM, Robinson SP, Satyaswaroop PG, and Jordan VC (1988) Contrasting actions of tamoxifen on endometrial and breast tumor growth in the athymic mouse. *Cancer Res* **48**:812–815.

Gottardis MM, Wagner RJ, Borden EC, and Jordan VC (1989b) Differential ability of antiestrogens to stimulate breast cancer cell (MCF-7) growth in vivo and in vitro. *Cancer Res* **49**:4765–4769.

Grootjans J, Kaser A, Kaufman RJ, and Blumberg RS (2016) The unfolded protein response in immunity and inflammation. *Nat Rev Immunol* **16**:469–484.

Haddow A (1970) David A. Karnofsky memorial lecture. Thoughts on chemical therapy. *Cancer* **26**:737–754.

Haddow A, Watkinson JM, Paterson E, and Koller PC (1944) Influence of synthetic oestrogens on advanced malignant disease. *Br Med J* **2**:393–398.

Hetz C (2012) The unfolded protein response: controlling cell fate decisions under ER stress and beyond. *Nat Rev Mol Cell Biol* **13**:89–102.

Hetz C and Saxena S (2017) ER stress and the unfolded protein response in neurodegeneration. *Nat Rev Neurol* **13**:477–491.

Holinka CF, Diczfalusy E, and Coelingh Bennink HJ (2008) Estetrol: a unique steroid in human pregnancy. *J Steroid Biochem Mol Biol* **110**:138–143.

Hosford SR, Shee K, Wells JD, Traphagen NA, Fields JL, Hampsch RA, Kettenbach AN, Demidenko E, and Miller TW (2019) Estrogen therapy induces an unfolded protein response to drive cell death in ER+ breast cancer. *Mol Oncol* **13**:1778–1794.

Ingle JN, Ahmann DL, Green SJ, Edmonson JH, Bisel HF, Kvols LK, Nichols WC, Creagan ET, Hahn RG, Rubin J, et al. (1981) Randomized clinical trial of diethylstilbestrol versus tamoxifen in postmenopausal women with advanced breast cancer. *N Engl J Med* **304**:16–21.

Iwase H, Yamamoto Y, Yamamoto-Ibusuki M, Murakami KI, Okumura Y, Tomita S, Inao T, Honda Y, Omoto Y, and Iyama KI (2013) Ethinylestradiol is beneficial for postmenopausal patients with heavily pre-treated metastatic breast cancer after prior aromatase inhibitor treatment: a prospective study. *Br J Cancer* **109**: 1537–1542.

Jiang SY, Wolf DM, Yingling JM, Chang C, and Jordan VC (1992) An estrogen receptor positive MCF-7 clone that is resistant to antiestrogens and estradiol. *Mol Cell Endocrinol* **90**:77–86.

Jordan VC (1984) Biochemical pharmacology of antiestrogen action. *Pharmacol Rev* **36**:245–276.
Jordan VC (2003) Tamoxifen: a most unlikely pioneering medicine. *Nat Rev Drug Discov* **2**:205–213.
Jordan VC (2008) The 38th David A. Karnofsky lecture: the paradoxical actions of estrogen in breast cancer--survival or death? *J Clin Oncol* **26**:3073–3082.
Jordan VC (2015) The new biology of estrogen-induced apoptosis applied to treat and prevent breast cancer. *Endocr Relat Cancer* **22**:R1–R31.
Jordan VC (2020) Molecular mechanism for breast cancer incidence in the women's health initiative. *Cancer Prev Res (Phila)* DOI: 10.1158/1940-6207.CAPR-20-0082 [published ahead of print].
Jordan VC and Allen KE (1980) Evaluation of the antitumour activity of the non-steroidal antioestrogen monohydroxytamoxifen in the DMBA-induced rat mammary carcinoma model. *Eur J Cancer* **16**:239–251.
Jordan VC and Assikis VJ (1995) Endometrial carcinoma and tamoxifen: clearing up a controversy. *Clin Cancer Res* **1**:467–472.
Jordan VC, Dix CJ, and Allen KE (1979) The effectiveness of long-term treatment in a laboratory model for adjuvant hormone therapy of breast cancer, in *Adjuvant Therpy of Cancer II* (Salmon SE and Jones SE 19–26, Greene and Stratton, New York.
Jordan VC, Koch R, Mittal S, and Schneider MR (1986) Oestrogenic and anti-oestrogenic actions in a series of triphenylbut-1-enes: modulation of prolactin synthesis in vitro. *Br J Pharmacol* **87**:217–223.
Jordan VC and Lieberman ME (1984) Estrogen-stimulated prolactin synthesis in vitro. Classification of agonist, partial agonist, and antagonist actions based on structure. *Mol Pharmacol* **26**:279–285.
Jordan VC, Lieberman ME, Cormier E, Koch R, Bagley JR, and Ruenitz PC (1984) Structural requirements for the pharmacological activity of nonsteroidal anti-estrogens in vitro. *Mol Pharmacol* **26**:272–278.
Kraus MH, Popescu NC, Amsbaugh SC, and King CR (1987) Overexpression of the EGF receptor-related proto-oncogene erbB-2 in human mammary tumor cell lines by different molecular mechanisms. *EMBO J* **6**:605–610.
Lemmo W (2016) Anti-estrogen withdrawal effect with raloxifene? A case report. *Integr Cancer Ther* **15**:245–249.
Lewis JS, Meeke K, Osipo C, Ross EA, Kidawi N, Li T, Bell E, Chandel NS, and Jordan VC (2005a) Intrinsic mechanism of estradiol-induced apoptosis in breast cancer cells resistant to estrogen deprivation. *J Natl Cancer Inst* **97**: 1746–1759.
Lewis JS, Osipo C, Meeke K, and Jordan VC (2005b) Estrogen-induced apoptosis in a breast cancer model resistant to long-term estrogen withdrawal. *J Steroid Biochem Mol Biol* **94**:131–141.
Lieberman ME, Gorski J, and Jordan VC (1983a) An estrogen receptor model to describe the regulation of prolactin synthesis by antiestrogens in vitro. *J Biol Chem* **258**:4741–4745.
Lieberman ME, Jordan VC, Fritsch M, Santos MA, and Gorski J (1983b) Direct and reversible inhibition of estradiol-stimulated prolactin synthesis by antiestrogens in vitro. *J Biol Chem* **258**:4734–4740.
Liu H, Lee ES, Gajdos C, Pearce ST, Chen B, Osipo C, Loweth J, McKian K, De Los Reyes A, Wing L, et al. (2003) Apoptotic action of 17beta-estradiol in raloxifene-resistant MCF-7 cells in vitro and in vivo. *J Natl Cancer Inst* **95**:1586–1597.
Lønning PE, Taylor PD, Anker G, Iddon J, Wie L, Jørgensen LM, Mella O, and Howell A (2001) High-dose estrogen treatment in postmenopausal breast cancer patients heavily exposed to endocrine therapy. *Breast Cancer Res Treat* **67**: 111–116.
Maly DJ and Papa FR (2014) Druggable sensors of the unfolded protein response. *Nat Chem Biol* **10**:892–901.
Maximov PY, Abderrahman B, Hawsawi YM, Chen Y, Foulds CE, Jain A, Malovannaya A, Fan P, Curpan RF, Han R, et al. (2020) The structure-function relationship of angular estrogens and estrogen receptor alpha to initiate estrogen-induced apoptosis in breast cancer cells. *Mol Pharmacol* **98**:24–37.
Maximov PY, Myers CB, Curpan RF, Lewis-Wambi JS, and Jordan VC (2010) Structure-function relationships of estrogenic triphenylethylenes related to endoxifen and 4-hydroxytamoxifen. *J Med Chem* **53**:3273–3283.
Molloy ME, White BE, Gherezghiher T, Michalsen BT, Xiong R, Patel H, Zhao H, Maximov PY, Jordan VC, Thatcher GR, et al. (2014) Novel selective estrogen mimics for the treatment of tamoxifen-resistant breast cancer. *Mol Cancer Ther* **13**: 2515–2526.
Murphy CS, Langan-Fahey SM, McCague R, and Jordan VC (1990a) Structure-function relationships of hydroxylated metabolites of tamoxifen that control the proliferation of estrogen-responsive T47D breast cancer cells in vitro. *Mol Pharmacol* **38**:737–743.
Murphy CS, Pink JJ, and Jordan VC (1990b) Characterization of a receptor-negative, hormone-nonresponsive clone derived from a T47D human breast cancer cell line kept under estrogen-free conditions. *Cancer Res* **50**:7285–7292.
Nishida M, Kasahara K, Kaneko M, Iwasaki H, and Hayashi K (1985) [Establishment of a new human endometrial adenocarcinoma cell line, Ishikawa cells, containing estrogen and progesterone receptors]. *Nippon Sanka Fujinka Gakkai Zasshi* **37**: 1103–1111.
Obiorah I, Sengupta S, Curpan R, and Jordan VC (2014) Defining the conformation of the estrogen receptor complex that controls estrogen-induced apoptosis in breast cancer. *Mol Pharmacol* **85**:789–799.
Obiorah IE and Jordan VC (2014) Differences in the rate of oestrogen-induced apoptosis in breast cancer by oestradiol and the triphenylethylene bisphenol. *Br J Pharmacol* **171**:4062–4072.
O'Regan RM, Hurley R, Sachdev JC, Bleeker J, Tonetti D, Thatcher GR, Venuti R, and Dudek AZ (2019) Phase I study of TTC-352 in patients with estrogen receptor-positive metastatic breast cancer (Abstract). *Cancer Res* **79**:CT051.
Pink JJ, Jiang SY, Fritsch M, and Jordan VC (1995) An estrogen-independent MCF-7 breast cancer cell line which contains a novel 80-kilodalton estrogen receptor-related protein. *Cancer Res* **55**:2583–2590.
Pisani P, Bray F, and Parkin DM (2002) Estimates of the world-wide prevalence of cancer for 25 sites in the adult population. *Int J Cancer* **97**:72–81.
Roehm E (2015) A reappraisal of women's health initiative estrogen-alone trial: long-term outcomes in women 50-59 Years of age. *Obstet Gynecol Int* **2015**:713295.
Rosenberg PS, Barker KA, and Anderson WF (2015) Estrogen receptor status and the future burden of invasive and in situ breast cancers in the United States. *J Natl Cancer Inst* **107**:djv159.
Schmidt M, Hönig A, Zimmerman Y, Verhoeven C, Almstedt K, Battista M, Lenhard HG, Krijgh J, and Bennink HC (2020) Estetrol for treatment of advanced ER+/HER2- breast cancer (Abstract). *Cancer Res* **80**:P5-11–15.
Sengupta S, Obiorah I, Maximov PY, Curpan R, and Jordan VC (2013) Molecular mechanism of action of bisphenol and bisphenol A mediated by oestrogen receptor alpha in growth and apoptosis of breast cancer cells. *Br J Pharmacol* **169**:167–178.
Sengupta S, Sharma CG, and Jordan VC (2010) Estrogen regulation of X-box binding protein-1 and its role in estrogen induced growth of breast and endometrial cancer cells. *Horm Mol Biol Clin Investig* **2**:235–243.
Sherman W, Beard HS, and Farid R (2006a) Use of an induced fit receptor structure in virtual screening. *Chem Biol Drug Des* **67**:83–84.
Sherman W, Day T, Jacobson MP, Friesner RA, and Farid R (2006b) Novel procedure for modeling ligand/receptor induced fit effects. *J Med Chem* **49**:534–553.
Shiau AK, Barstad D, Loria PM, Cheng L, Kushner PJ, Agard DA, and Greene GL (1998) The structural basis of estrogen receptor/coactivator recognition and the antagonism of this interaction by tamoxifen. *Cell* **95**:927–937.
Singer CF, Bennink HJ, Natter C, Steurer S, Rudas M, Moinfar F, Appels N, Visser M, and Kubista E (2014) Antiestrogenic effects of the fetal estrogen estetrol in women with estrogen-receptor positive early breast cancer. *Carcinogenesis* **35**: 2447–2451.
Song RX, Mor G, Naftolin F, McPherson RA, Song J, Zhang Z, Yue W, Wang J, and Santen RJ (2001) Effect of long-term estrogen deprivation on apoptotic responses of breast cancer cells to 17beta-estradiol. *J Natl Cancer Inst* **93**: 1714–1723.
Verhoeven C, Schmidt M, Hönig A, Dünnebacke J, Dutman E, Krijgh J, and Coelingh-Bennink H (2018) Abstract OT1-04-01: Estetrol for treatment of advanced ER+ breast cancer. DOI: 10.1158/1538-7445.SABCS17-OT1-04-01
Vogel VG, Costantino JP, Wickerham DL, Cronin WM, Cecchini RS, Atkins JN, Bevers TB, Fehrenbacher L, Pajon ER Jr., Wade JL III, et al. National Surgical Adjuvant Breast and Bowel Project (NSABP) (2006) Effects of tamoxifen vs raloxifene on the risk of developing invasive breast cancer and other disease outcomes: the NSABP Study of Tamoxifen and Raloxifene (STAR) P-2 trial [published correction appears in *JAMA* (2006) 296:2926; *JAMA* (2007) 298:973]. *JAMA* **295**: 2727–2741.
Wolf DM and Jordan VC (1993) A laboratory model to explain the survival advantage observed in patients taking adjuvant tamoxifen therapy. *Recent Results Cancer Res* **127**:23–33.
Xiong R, Patel HK, Gutgesell LM, Zhao J, Delgado-Rivera L, Pham TND, Zhao H, Carlson K, Martin T, Katzenellenbogen JA, et al. (2016) Selective human estrogen receptor partial agonists (ShERPAs) for tamoxifen-resistant breast cancer. *J Med Chem* **59**:219–237.
Yao K, Lee ES, Bentrem DJ, England G, Schafer JI, O'Regan RM, and Jordan VC (2000) Antitumor action of physiological estradiol on tamoxifen-stimulated breast tumors grown in athymic mice. *Clin Cancer Res* **6**:2028–2036.

Address correspondence to: V. Craig Jordan, Department of Breast Medical Oncology, University of Texas MD Anderson Cancer Center, 1515 Holcombe Blvd., Unit 1354, Houston, TX 77030. E-mail: VCJordan@mdanderson.org

Abderrahman et al. Pharmacology and Molecular Mechanisms of Clinically-Relevant Estrogen Estetrol and Estrogen Mimic BMI-135 for Endocrine-Resistant Breast Cancer Treatment. Molecular Pharmacology 2020. (MOLPHARM-AR-2020-000054)

Supplemental Table. 1. Validation of all cell lines (MCF-7:WS8, T47D:A18, MCF-7:PF, BT-474, ZR-75-1, MCF-7:5C, MCF-7:2A, and MCF-7:RAL).

Supplemental Fig. 1. Cell viability and proliferation assays in multiple human BC cell lines with test compounds over various time frames. (A) Effects of test compounds alone after 7 days of treatment (percent DNA of vehicle versus test compounds' days of treatment) in MCF-7:WS8. (B) Effects of test compounds alone after 7 days of treatment in T47D:A18. (C) Effects of test compounds alone after 7 days of treatment in MCF-7:PF. (D) Effects of test compounds alone after 14 days of treatment in MCF-7:5C. (E) Effects of test compounds alone after 14 days of treatment in MCF-7:2A. (F) Effects of test compounds alone after 21 days of treatment in MCF-7:RAL. Concetration of test compounds: 1 nM for E_2, and 1 µM for the rest. Data are mean ± SD from three independent experiments performed in triplicate analyzed by one-way ANOVA.

Supplemental Fig. 2. Cell viability and proliferation assays in multiple human BC cell lines with test compounds in combination with 4OHT and endoxifen. (A) One-week cell viability and proliferation assay combing E_2, E_4, and BMI-135 with 4OHT and endoxifen in MCF-7:5C cells. (B) Two-week cell viability and proliferation assay combing E_2, E_4, and BMI-135 with 4OHT and endoxifen in MCF-7:2A cells. (C) Three-week cell viability and proliferation assay combing E_2, E_4, and BMI-135 with 4OHT and endoxifen in MCF-7:RAL cells. Concetration of test compounds: 1 nM for E_2, and 1 µM for the rest. Data are mean ± SD from three independent experiments performed in triplicate analyzed by one-way ANOVA.

Supplemental Fig. 3. MD structural analysis. (A) Plots showing the RMSD evolution of trajectories and the root mean square fluctuation (RMSF in Å) of each residue in ERα:LBD WT bound complexes: E_2 (yellow), BMI-135 (blue), and BPTPE (backbone), calculated for backbone atoms during the 50ns simulation time. (B) The ligands' fluctuation during the simulation time (expressed as RMSD) is calculated against the ligand as reference (above image), and when the protein is first aligned to the reference protein structure, and, then, the ligand displacement is calculated (lower image).

Supplemental Fig. 4. Human UPR RT^2 PCR profiler PCR arrays, proliferation assays, and annexin V staining, in MCF-7:5C cells with 3-day, 7-day, 8-day, and 14-day BPTPE treatments. (A) A heat map of 7-day BPTPE treatment, providing a visualization of the fold changes in expression between the select groups (from left to right; BPTPE, and vehicle, respectively), for every gene in the array in the context of the array layout. (B) A volcano plot of 7-day BPTPE treatment. (C) A scatter plot of 3-day BPTPE treatment. (D) Effects of BPTPE alone after 14 days of treatment. (E) Flow cytometry of 8-day BPTPE treatment. (B and C) Green represents down-regulated, black unchanged, and red up-regulated. Data are mean ± SD from three independent experiments performed in triplicate analyzed by one-way ANOVA.

Supplemental Fig. 5. Representation of statistically-significant UPR genes that are under-or-over expressed in MCF-7:5C cells treated with test compounds at specific time points. (A) MCF-7:5C cells with 48-hour E_2 treatment. (B) MCF-7:5C cells with 48-hour E_4 treatment. (C) MCF-7:5C cells with 48-hour BMI-135 treatment. (D) MCF-7:5C cells with 72-hour BMI-135 treatment. (E) MCF-7:5C cells with 3-day BPTPE treatment. (F) MCF-7:5C cells with 7-day BPTPE treatment.

Supplemental Fig. 6. Detection of UPR in live MCF-7:5C cells using ThT fluorescent dye after 48-hour treatments as measured by the ZEISS Celldiscoverer 7 microscope. (A) Hoechst 33342 dye single panel (blue). (B) ThT dye single panel (green). (C) A merge or co-localization ThT+Hoechst 33342 dyes panel (blue and green). Scale bar = 50 μM. ThT relative intensity/cell, per treatment, is the mean of 3 biological repeats with SD (Table 2A).

Supplemental Fig. 7. Flow cytometry in MCF-7:5C cells with E_2 and E_4 plus a PERK inhibitor or an IRE1α inhibitor after 72-hour-treatments. (A) MCF-7:5C cells were treated with vehicle control, 10 μM GSK G797800, 1 nM E_2+10 μM GSK G797800, and 1 μM E_4+10 μM GSK G797800. (B) MCF-7:5C cells were treated with vehicle control, 1 μM E_4, 20 μM MKC-3946, and 1 μM E4+20 μM MKC-3946. Data are mean ± SD from three independent experiments analyzed by one-way ANOVA. A and B, ***$P < 0.001$.

Supplemental Fig. 8. Flow cytometry in MCF-7:2A cells after 9-and-13-day treatments, and in MCF-7:5C cells after 72-hour treatments. (A) MCF-7:2A cells were treated with vehicle control, 1 nM E_2, and 1 μM E_4 for 9 days. (B) MCF-7:2A cells were treated with vehicle control, and 1 μM BMI-135 for 13 days. (C) MCF-7:2A cells were treated with vehicle control, and 1 μM BMI-135 for 9 days. (D) MCF-7:5C cells were treated with vehicle control, and 1 μM BMI-135 for 72 hours. Data are mean ± SD from three independent experiments analyzed by one-way ANOVA. A-D, ***$P < 0.001$.

Supplemental Fig. 9. Flow cytometry in MCF-7:RAL cells after 14-day, 17-day, and 21-day treatments. (A) MCF-7:RAL cells were treated with vehicle control, 1 μM raloxifene, 1 μM 4OHT, 1 nM E_2, and 1 μM E_4 for 14 days. (B) MCF-7:RAL cells were treated with vehicle control, and 1 μM BMI-135 for 17 days. (C) MCF-7:RAL cells were treated with vehicle control, and 1 μM BMI-135 for 14 days. (D) MCF-7:RAL cells were treated with vehicle

control, and 1 μM ICI for 21 days. Data are mean ± SD from three independent experiments analyzed by one-way ANOVA. A-D, ***$P < 0.001$.

Supplemental Fig. 10. Analysis of local fluctuations in the binding site of BMI-135 together with the binding alignment and specific interactions of the ligands in the binding pocket of ERα. (A) The root-mean-square fluctuations (RMSF) were calculated based on backbone atoms, and side chains for amino acids lining the binding site. (B-E) 2D schematic representations of the detailed ligand atom interactions and (F-I) close views of the binding site of ERα with its ligand: E_2 (B, F), E_4 (C, G), BMI-135 (D, H), and BPTPE (E, I). There is a core of common residues involved in interactions with all ligands: Glu353 and Arg394 (H-bonds with the 3-OH group), Phe404 (π-π stacking), and Leu346, Leu387, Ala350, Ile424, and Leu525 (hydrophobic contacts). In the 2D representations (B-E), the hydrophobic amino acids are colored in green, polar in light blue, positively-charged in red, and negatively-charged in blue. For contacts, the following color code is used: H-bonds in magenta, and π-π stacking in green. In the 3D representations (F-I), hydrophobic contacts are colored in light magenta, and π-π stacking contacts in dark magenta, H-bonds in green, and water bridges in blue.

Supplemental Fig. 11. Time-line representations of the monitored interactions and contacts (H-bonds, hydrophobic, ionic, and water bridges) throughout the simulation. The panels show which residues interact with the ligands: E_2 (A), BMI-135 (B), and BPTPE (C), in each trajectory frame during the 50ns simulation time. Residues making more than one specific contact with the ligand are represented in darker shades of orange.

Cytogenetics and Cell Authentication core

CCAC database is a comprehensive databases of short tandem repeat (STR) profiles, The database includes profiles from 20 public database/ publications and the cell lines developed by MD Anderson research labs.
The database contains over 4500 unique human cancer cell line STR profiles, one of the largest cancer cell line STR online search database in the world

For questions please contact Xuesong Li (713)-792-6833 , Xsli@mdanderson.org

THE UNIVERSITY OF TEXAS
MD Anderson Cancer Center
Making Cancer History®

Annual cell line authentication is required by
UTMDACC INSTITUTIONAL POLICY # ACA1044

SET 507	11/18/2019

Expiration date: 11/18/2020

Source	Sample_Name	AMEL	CSF1PO	D13S317	D16S539	D18S51	D21S11	D3S1358	D5S818	D7S820	D8S1179	FGA	TH01	TPOX	vWA	Comments
Balkees Abderrahman	MCF-7-2A	X	10	11	11,12	14	30	15,16	12	8,9	10,14	23,25	6	9,12	14,15	
Balkees Abderrahman	MCF-7-5C	X	10	11	11,12	14	30	16,17	12	8,9	10,14	23,25	6	9,12	14,15	
Balkees Abderrahman	MCF-7-ATCC	X	10	11	11,12	14	30	16	11,12	8,9	10,14	23,25	6	9,12	14,15	
Balkees Abderrahman	MCF-7-LCCC1	X	10	11	11,12	14	30	16	11,12	8,9	10,14	23,25	6	9,12	14,15	
Balkees Abderrahman	MCF-7-LCCC2	X	10	11	11,12	14	29,30	16	12	8,9	10,14	23,25	6	9,12	14,15	
Balkees Abderrahman	MCF7-LCCC9	X	10	11	11,12	14	30	16	12	8,9	10,14	23,25	6	9,12	14,15	
Balkees Abderrahman	MCF-7-PF	X	10	11	11,12	14	30	16,17	12	8,9	10,14	23,25	6	9,12	14,15	
Balkees Abderrahman	MCF-7-RAL	X	10	11	11,12	14	30	16	12	8,9	10,14	23,24,25	6	9,12	14,15	
Balkees Abderrahman	MCF-7-WS8	X	10	11	11,12	14	30	16	12	8,9	10,14	23,25	6	9,12	15	
Public database_NCI	MCF7	X	10	11	11,12	14	30	16	11,12	8,9	10,14	23,25	6	9,12	14,15	MATCH

Source	Sample_Name	AMEL	CSF1PO	D13S317	D16S539	D18S51	D21S11	D3S1358	D5S818	D7S820	D8S1179	FGA	TH01	TPOX	vWA	Comments
Balkees Abderrahman	BT474	X	10,11	11	9,11	13,18	28,32.2	17	11,13	9,12	10,12	22,25	7	8	15,16	
Public database_ATCC	BT474	X	10,11	11	9,11	13,18	28,32.2	17	11,13	9,12	10,12	22,25	7	8	15,16	MATCH

Source	Sample_Name	AMEL	CSF1PO	D13S317	D16S539	D18S51	D21S11	D3S1358	D5S818	D7S820	D8S1179	FGA	TH01	TPOX	vWA	Comments
Balkees Abderrahman	T47D-A18	X	11	12	10	17	28,31	15,17	12	11	13	23	6	11	14	
Public database_NCI	T47D	X	11,13	12	10	17	28,31	15,17	12	11	13	23	6	11	14	MATCH

Source	Sample_Name	AMEL	CSF1PO	D13S317	D16S539	D18S51	D21S11	D3S1358	D5S818	D7S820	D8S1179	FGA	TH01	TPOX	vWA	Comments
Balkees Abderrahman	ZR-75-1	X	10,11	9	11	13,14	31	15,16	13	10,11	11,13	20,22	7,9.3	8		signal a little low
Public database_ATCC	ZR75-1	X	10,11	9	11,12	13,14	31	15,16	13	10	11,13	20,22	7,9.3	8	16,18	MATCH

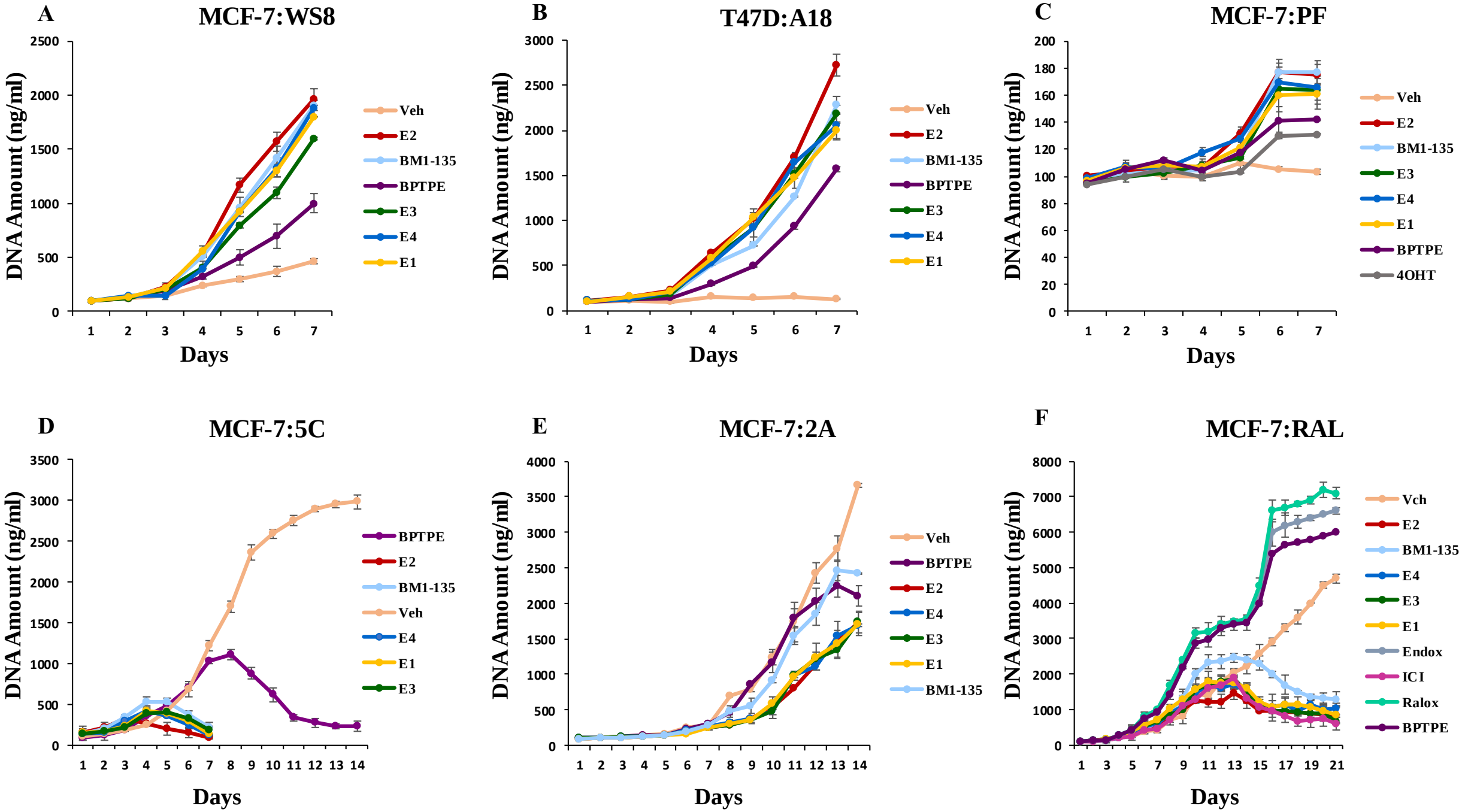
A
MCF-7:WS8
DNA Amount (ng/ml)
Days
Veh
E2
BM1-135
BPTPE
E3
E4
E1
B
T47D:A18
DNA Amount (ng/ml)
Days
Veh
E2
BM1-135
BPTPE
E3
E4
E1
C
MCF-7:PF
DNA Amount (ng/ml)
Days
Veh
E2
BM1-135
E3
E4
E1
BPTPE
4OHT
D
MCF-7:5C
DNA Amount (ng/ml)
Days
BPTPE
E2
BM1-135
Veh
E4
E1
E3
E
MCF-7:2A
DNA Amount (ng/ml)
Days
Veh
BPTPE
E2
E4
E3
E1
BM1-135
F
MCF-7:RAL
DNA Amount (ng/ml)
Days
Vch
E2
BM1-135
E4
E3
E1
Endox
ICI
Ralox
BPTPE

S Fig. 2

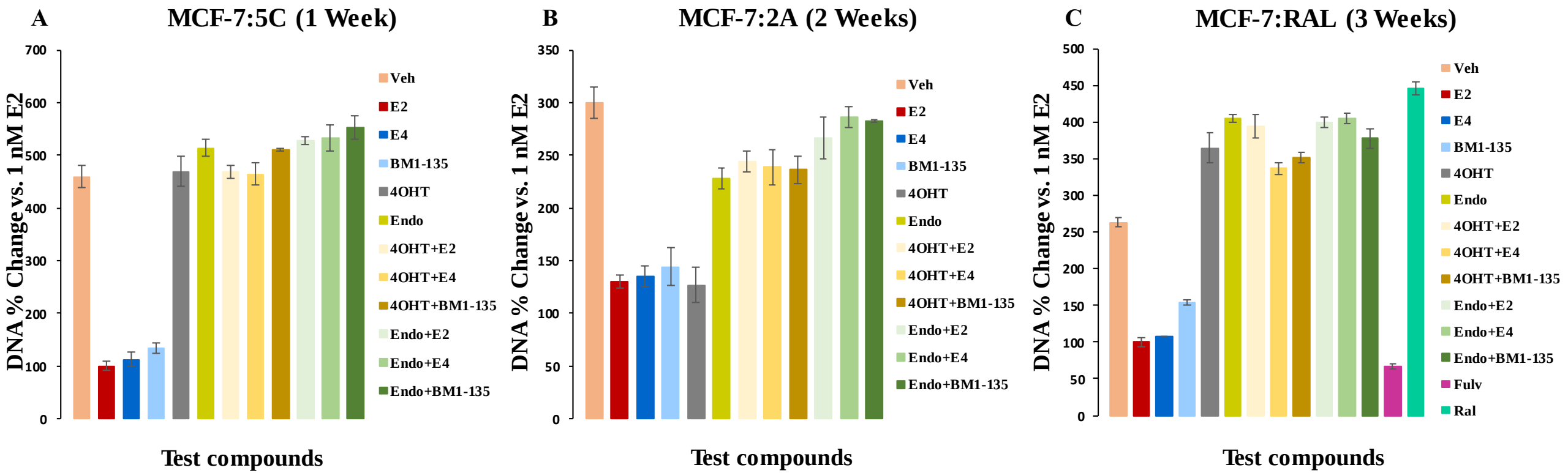
A
MCF-7:5C (1 Week)
DNA % Change vs. 1 nM E2
Test compounds
B
MCF-7:2A (2 Weeks)
DNA % Change vs. 1 nM E2
Test compounds
C
MCF-7:RAL (3 Weeks)
DNA % Change vs. 1 nM E2
Test compounds
Veh
E2
E4
BM1-135
4OHT
Endo
4OHT+E2
4OHT+E4
4OHT+BM1-135
Endo+E2
Endo+E4
Endo+BM1-135
Fulv
Ral

S Fig. 3

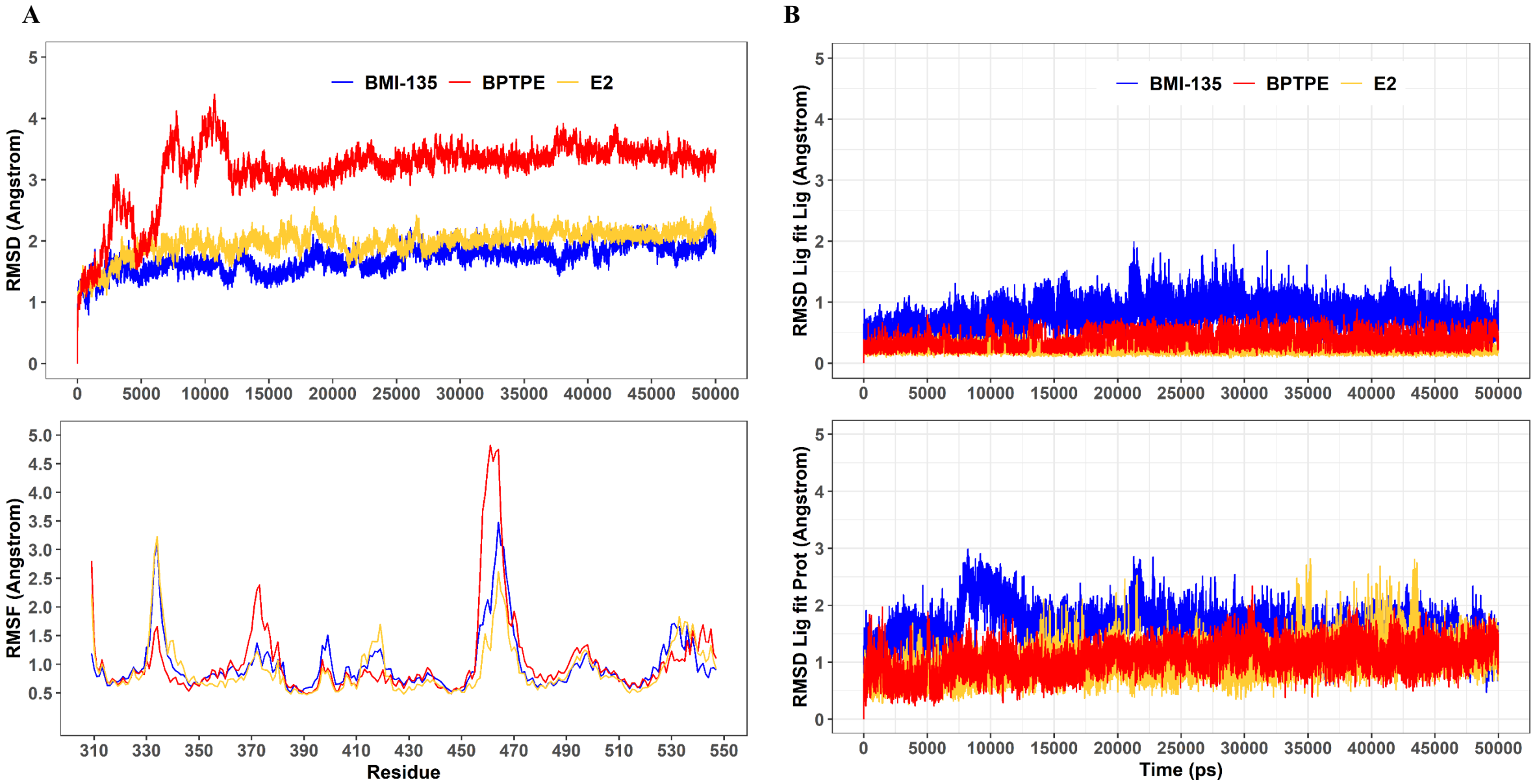
A
B
BMI-135
BPTPE
E2
RMSD (Angstrom)
RMSD Lig fit Lig (Angstrom)
RMSF (Angstrom)
RMSD Lig fit Prot (Angstrom)
Residue
Time (ps)

S Fig. 4

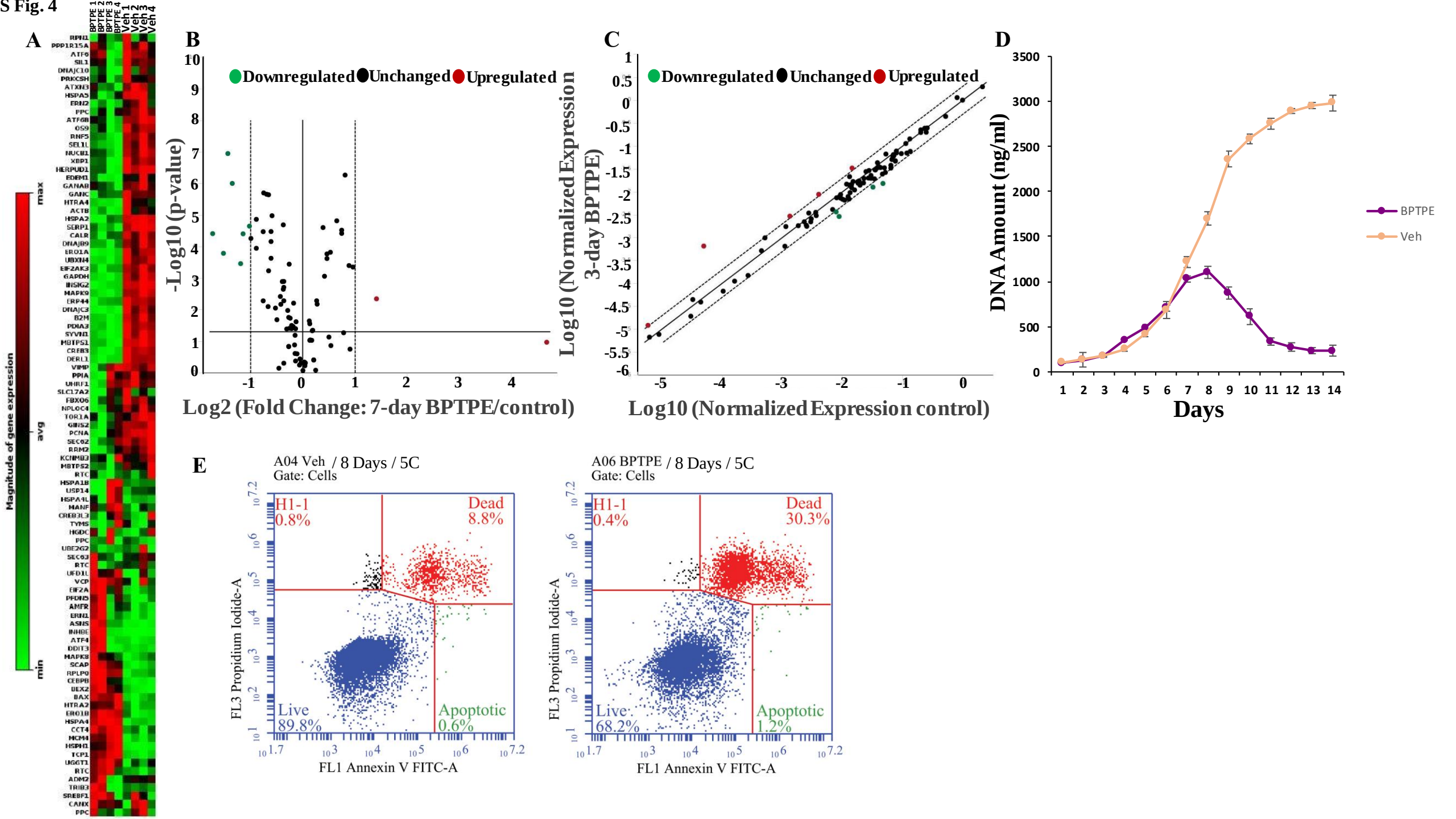
A
BPTPE 1
BPTPE 2
BPTPE 3
BPTPE 4
Veh 1
Veh 2
Veh 3
Veh 4
max
avg
min
Magnitude of gene expression
B
Downregulated
Unchanged
Upregulated
-Log10 (p-value)
Log2 (Fold Change: 7-day BPTPE/control)
C
Downregulated
Unchanged
Upregulated
Log10 (Normalized Expression 3-day BPTPE)
Log10 (Normalized Expression control)
D
DNA Amount (ng/ml)
Days
BPTPE
Veh
E
A04 Veh / 8 Days / 5C
Gate: Cells
H1-1
0.8%
Dead
8.8%
Live
89.8%
Apoptotic
0.6%
FL3 Propidium Iodide-A
FL1 Annexin V FITC-A
A06 BPTPE / 8 Days / 5C
Gate: Cells
H1-1
0.4%
Dead
30.3%
Live
68.2%
Apoptotic
1.2%
FL3 Propidium Iodide-A
FL1 Annexin V FITC-A

S Fig. 5

A

E2 48 Hours

Position	Gene Symbol	Fold Regulation	p-Value
A10	CEBPB	3.28	0.000006
C10	HTRA4	-6.55	0.000020
D02	MAPK9	-2.01	0.000002
D03	MBTPS1	-3.29	0.000000
E08	SERP1	-2.15	0.000029
E11	SYVN1	-2.21	0.000004
F09	ADM2	-3.10	0.000387
G03	HERPUD1	-5.49	0.000000
G04	INHBE	18.07	0.000031
G10	TRIB3	-3.04	0.000008
H02	B2M	-2.37	0.000014

B

E4 48 Hours

Position	Gene Symbol	Fold Regulation	p-Value
A10	CEBPB	2.96	0.000000
C10	HTRA4	-8.00	0.000014
D03	MBTPS1	-3.18	0.000000
E09	SIL1	-2.12	0.000001
E11	SYVN1	-2.40	0.000002
F09	ADM2	-2.31	0.000703
G03	HERPUD1	-4.60	0.000000
G04	INHBE	15.70	0.000003
G09	SLC17A2	-2.06	0.023929
G10	TRIB3	-3.06	0.000007

C

BMI-135 48 Hours

Position	Gene Symbol	Fold Regulation	p-Value
A10	CEBPB	3.08	0.000001
B04	EDEM1	-2.08	0.000005
B06	EIF2AK3	-9.46	0.038125
C10	HTRA4	-4.60	0.000036
D03	MBTPS1	-3.26	0.000000
E08	SERP1	-2.07	0.000000
E11	SYVN1	-2.16	0.000003
F09	ADM2	-2.66	0.000307
G03	HERPUD1	-5.15	0.000000
G04	INHBE	19.75	0.000000
G10	TRIB3	-2.78	0.000011

D

BMI-135 72 Hours

Position	Gene Symbol	Fold Regulation	p-Value
A10	CEBPB	3.97	0.000000
B07	ERN1	2.05	0.000000
B10	ERO1B	2.78	0.000050
C03	HSPA1B	2.76	0.000000
C04	HSPA2	-2.18	0.000017
C10	HTRA4	-4.16	0.000095
D03	MBTPS1	-2.39	0.000001
D11	PPP1R15A	2.57	0.000000
E06	SEL1L	-2.78	0.001751
F11	BEX2	2.89	0.000005
F12	DDIT3	3.53	0.000029
G03	HERPUD1	-3.51	0.000158
G04	INHBE	73.77	0.000000
H07	RTC	-3.33	0.000114

E

BPTPE Day 3

Position	Gene Symbol	Fold Regulation	p-Value
A10	CEBPB	2.26	0.007173
B06	EIF2AK3	-2.15	0.000004
C04	HSPA2	-3.08	0.000162
E06	SEL1L	-3.11	0.001346
F11	BEX2	2.19	0.000630
G03	HERPUD1	-2.57	0.002079

F

BPTPE Day 7

Position	Gene Symbol	Fold Regulation	p-Value
A10	CEBPB	2.67	0.004554
C04	HSPA2	-3.30	0.000039
C11	INSIG2	-2.69	0.000000
D03	MBTPS1	-2.54	0.000001
G01	DNAJB9	-2.29	0.000348
G03	HERPUD1	-2.86	0.000164
H02	B2M	-2.21	0.000040
H03	GAPDH	-2.02	0.000023

S Fig. 6

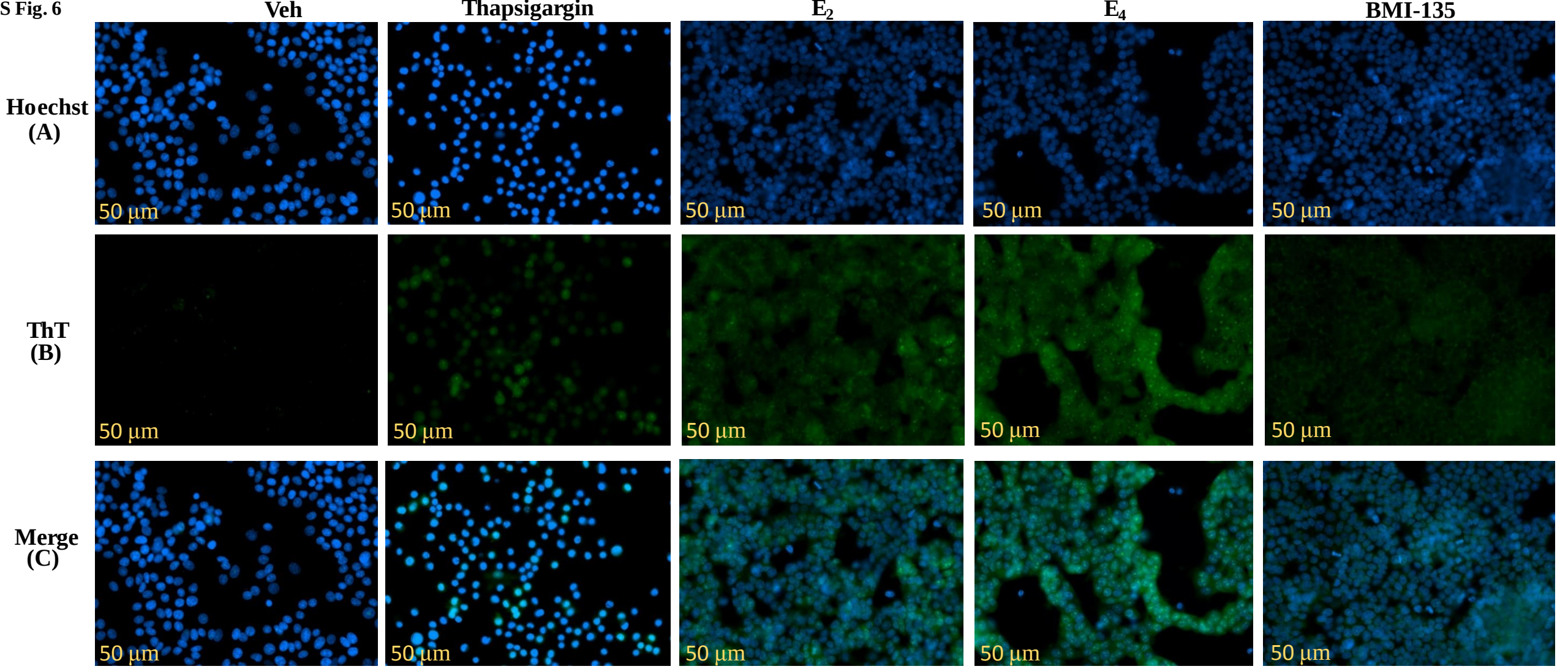

S Fig. 7

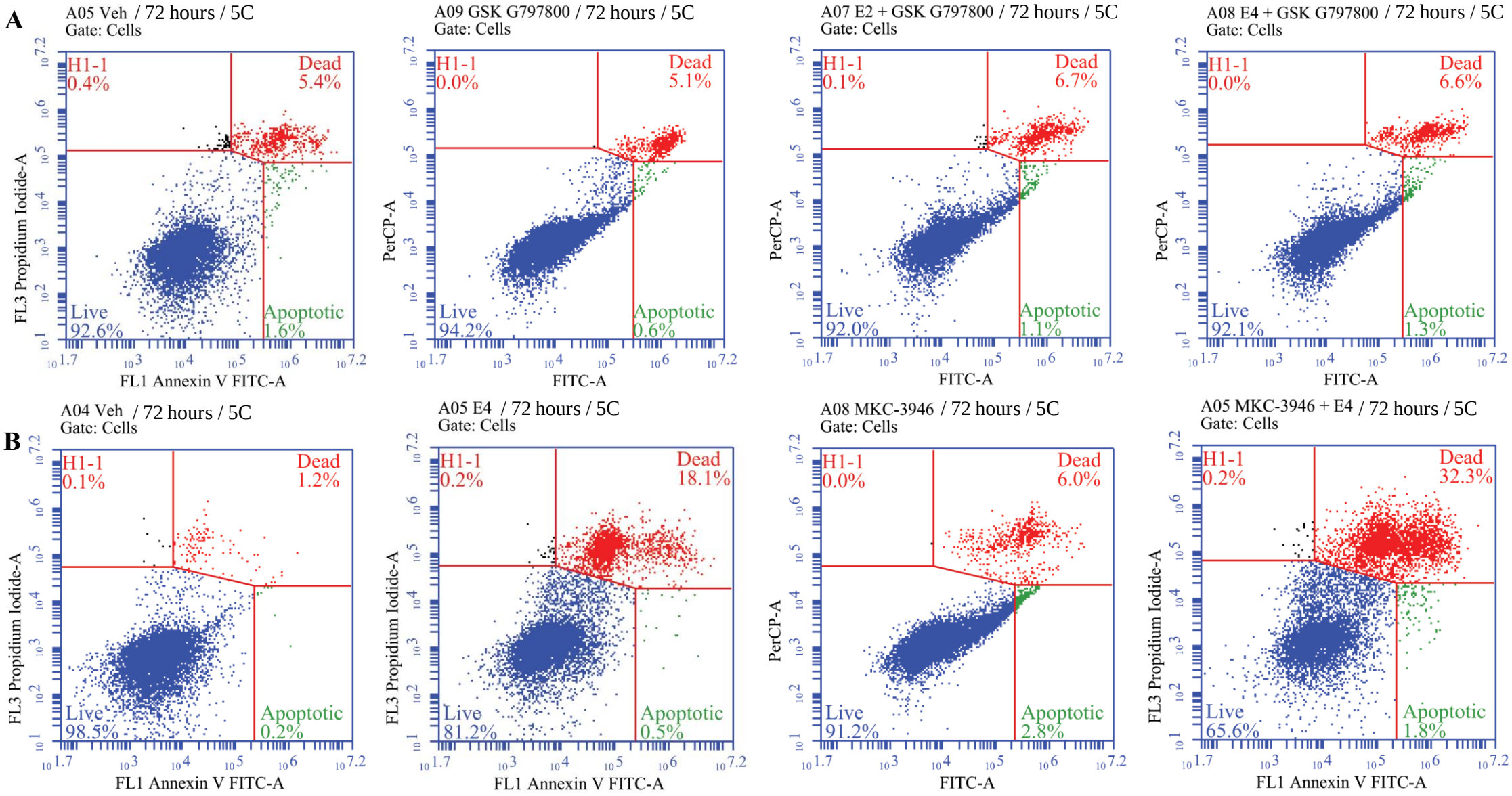
A
A05 Veh / 72 hours / 5C
Gate: Cells
H1-1
0.4%
Dead
5.4%
Live
92.6%
Apoptotic
1.6%
FL3 Propidium Iodide-A
FL1 Annexin V FITC-A
A09 GSK G797800 / 72 hours / 5C
Gate: Cells
H1-1
0.0%
Dead
5.1%
Live
94.2%
Apoptotic
0.6%
PerCP-A
FITC-A
A07 E2 + GSK G797800 / 72 hours / 5C
Gate: Cells
H1-1
0.1%
Dead
6.7%
Live
92.0%
Apoptotic
1.1%
PerCP-A
FITC-A
A08 E4 + GSK G797800 / 72 hours / 5C
Gate: Cells
H1-1
0.0%
Dead
6.6%
Live
92.1%
Apoptotic
1.3%
PerCP-A
FITC-A
B
A04 Veh / 72 hours / 5C
Gate: Cells
H1-1
0.1%
Dead
1.2%
Live
98.5%
Apoptotic
0.2%
FL3 Propidium Iodide-A
FL1 Annexin V FITC-A
A05 E4 / 72 hours / 5C
Gate: Cells
H1-1
0.2%
Dead
18.1%
Live
81.2%
Apoptotic
0.5%
FL3 Propidium Iodide-A
FL1 Annexin V FITC-A
A08 MKC-3946 / 72 hours / 5C
Gate: Cells
H1-1
0.0%
Dead
6.0%
Live
91.2%
Apoptotic
2.8%
PerCP-A
FITC-A
A05 MKC-3946 + E4 / 72 hours / 5C
Gate: Cells
H1-1
0.2%
Dead
32.3%
Live
65.6%
Apoptotic
1.8%
FL3 Propidium Iodide-A
FL1 Annexin V FITC-A

S Fig. 8

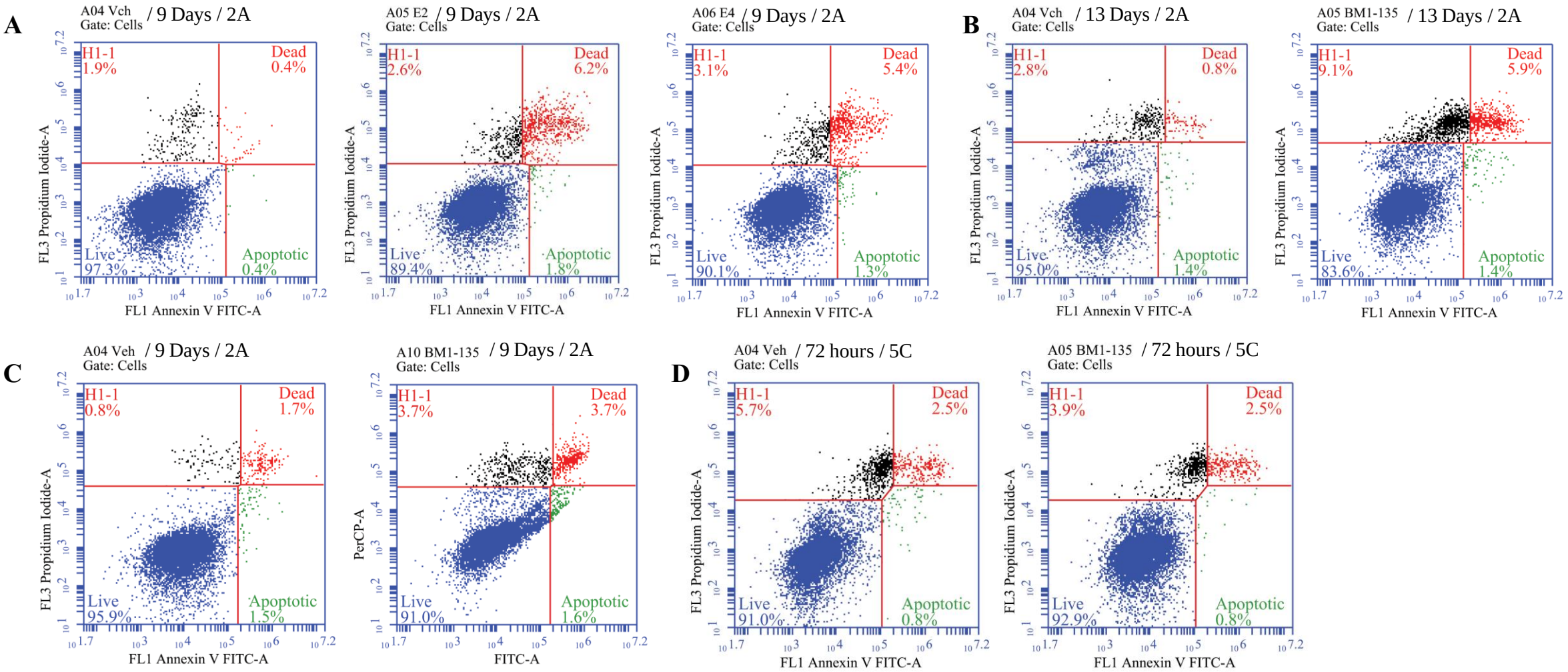
A
A04 Vch / 9 Days / 2A
Gate: Cells
H1-1
1.9%
Dead
0.4%
Live
97.3%
Apoptotic
0.4%
A05 E2 / 9 Days / 2A
Gate: Cells
H1-1
2.6%
Dead
6.2%
Live
89.4%
Apoptotic
1.8%
A06 E4 / 9 Days / 2A
Gate: Cells
H1-1
3.1%
Dead
5.4%
Live
90.1%
Apoptotic
1.3%
B
A04 Vch / 13 Days / 2A
Gate: Cells
H1-1
2.8%
Dead
0.8%
Live
95.0%
Apoptotic
1.4%
A05 BM1-135 / 13 Days / 2A
Gate: Cells
H1-1
9.1%
Dead
5.9%
Live
83.6%
Apoptotic
1.4%
FL3 Propidium Iodide-A
FL1 Annexin V FITC-A
C
A04 Veh / 9 Days / 2A
Gate: Cells
H1-1
0.8%
Dead
1.7%
Live
95.9%
Apoptotic
1.5%
A10 BM1-135 / 9 Days / 2A
Gate: Cells
H1-1
3.7%
Dead
3.7%
Live
91.0%
Apoptotic
1.6%
PerCP-A
FITC-A
D
A04 Veh / 72 hours / 5C
Gate: Cells
H1-1
5.7%
Dead
2.5%
Live
91.0%
Apoptotic
0.8%
A05 BM1-135 / 72 hours / 5C
Gate: Cells
H1-1
3.9%
Dead
2.5%
Live
92.9%
Apoptotic
0.8%

S Fig. 9

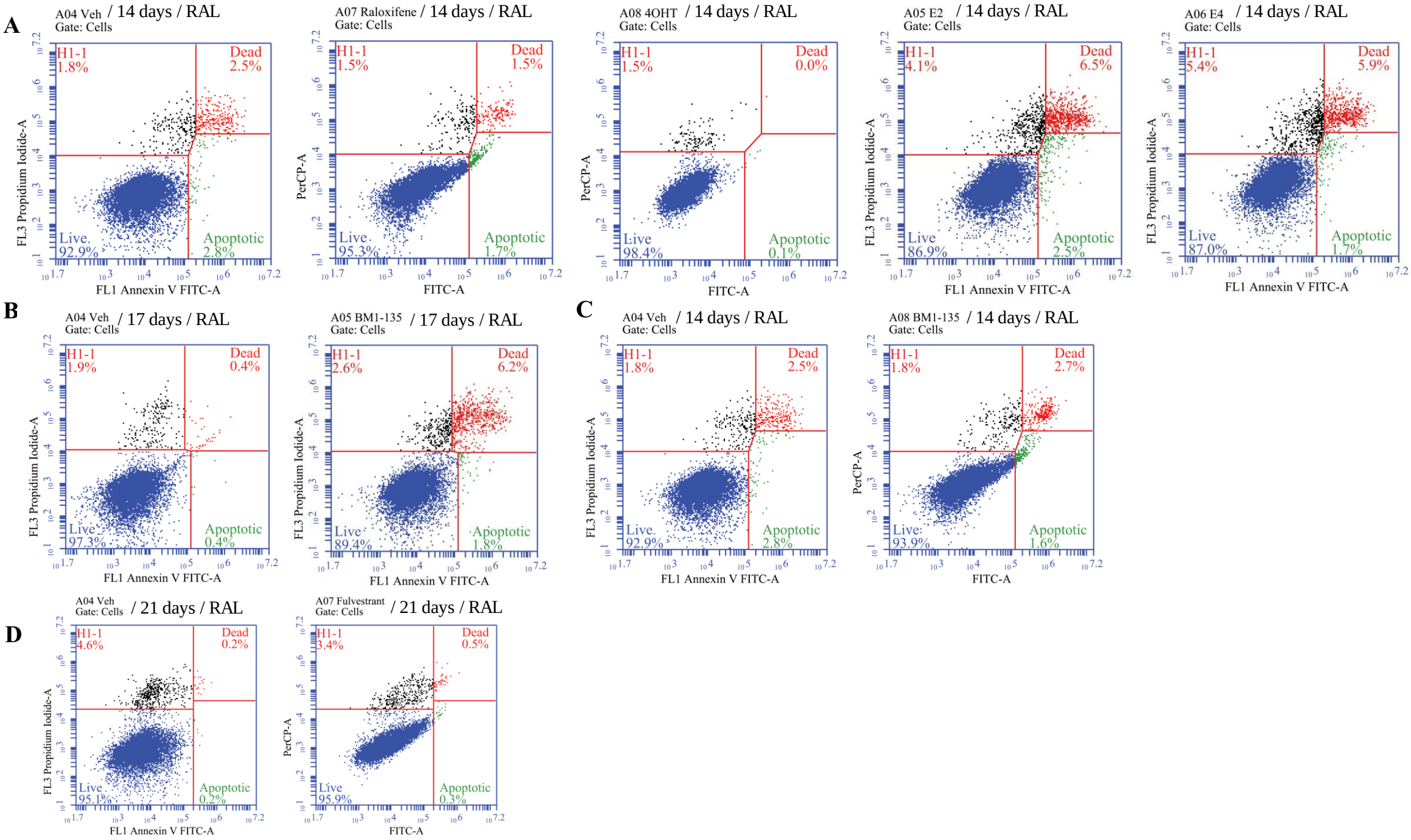
A
A04 Veh / 14 days / RAL
Gate: Cells
H1-1
1.8%
Dead
2.5%
Live
92.9%
Apoptotic
2.8%
FL3 Propidium Iodide-A
FL1 Annexin V FITC-A
A07 Raloxifene / 14 days / RAL
Gate: Cells
H1-1
1.5%
Dead
1.5%
Live
95.3%
Apoptotic
1.7%
PerCP-A
FITC-A
A08 4OHT / 14 days / RAL
Gate: Cells
H1-1
1.5%
Dead
0.0%
Live
98.4%
Apoptotic
0.1%
PerCP-A
FITC-A
A05 E2 / 14 days / RAL
Gate: Cells
H1-1
4.1%
Dead
6.5%
Live
86.9%
Apoptotic
2.5%
FL3 Propidium Iodide-A
FL1 Annexin V FITC-A
A06 E4 / 14 days / RAL
Gate: Cells
H1-1
5.4%
Dead
5.9%
Live
87.0%
Apoptotic
1.7%
FL3 Propidium Iodide-A
FL1 Annexin V FITC-A
B
A04 Veh / 17 days / RAL
Gate: Cells
H1-1
1.9%
Dead
0.4%
Live
97.3%
Apoptotic
0.4%
FL3 Propidium Iodide-A
FL1 Annexin V FITC-A
A05 BM1-135 / 17 days / RAL
Gate: Cells
H1-1
2.6%
Dead
6.2%
Live
89.4%
Apoptotic
1.8%
FL3 Propidium Iodide-A
FL1 Annexin V FITC-A
C
A04 Veh / 14 days / RAL
Gate: Cells
H1-1
1.8%
Dead
2.5%
Live
92.9%
Apoptotic
2.8%
FL3 Propidium Iodide-A
FL1 Annexin V FITC-A
A08 BM1-135 / 14 days / RAL
Gate: Cells
H1-1
1.8%
Dead
2.7%
Live
93.9%
Apoptotic
1.6%
PerCP-A
FITC-A
D
A04 Veh / 21 days / RAL
Gate: Cells
H1-1
4.6%
Dead
0.2%
Live
95.1%
Apoptotic
0.2%
FL3 Propidium Iodide-A
FL1 Annexin V FITC-A
A07 Fulvestrant / 21 days / RAL
Gate: Cells
H1-1
3.4%
Dead
0.5%
Live
95.9%
Apoptotic
0.3%
PerCP-A
FITC-A

S Fig. 10

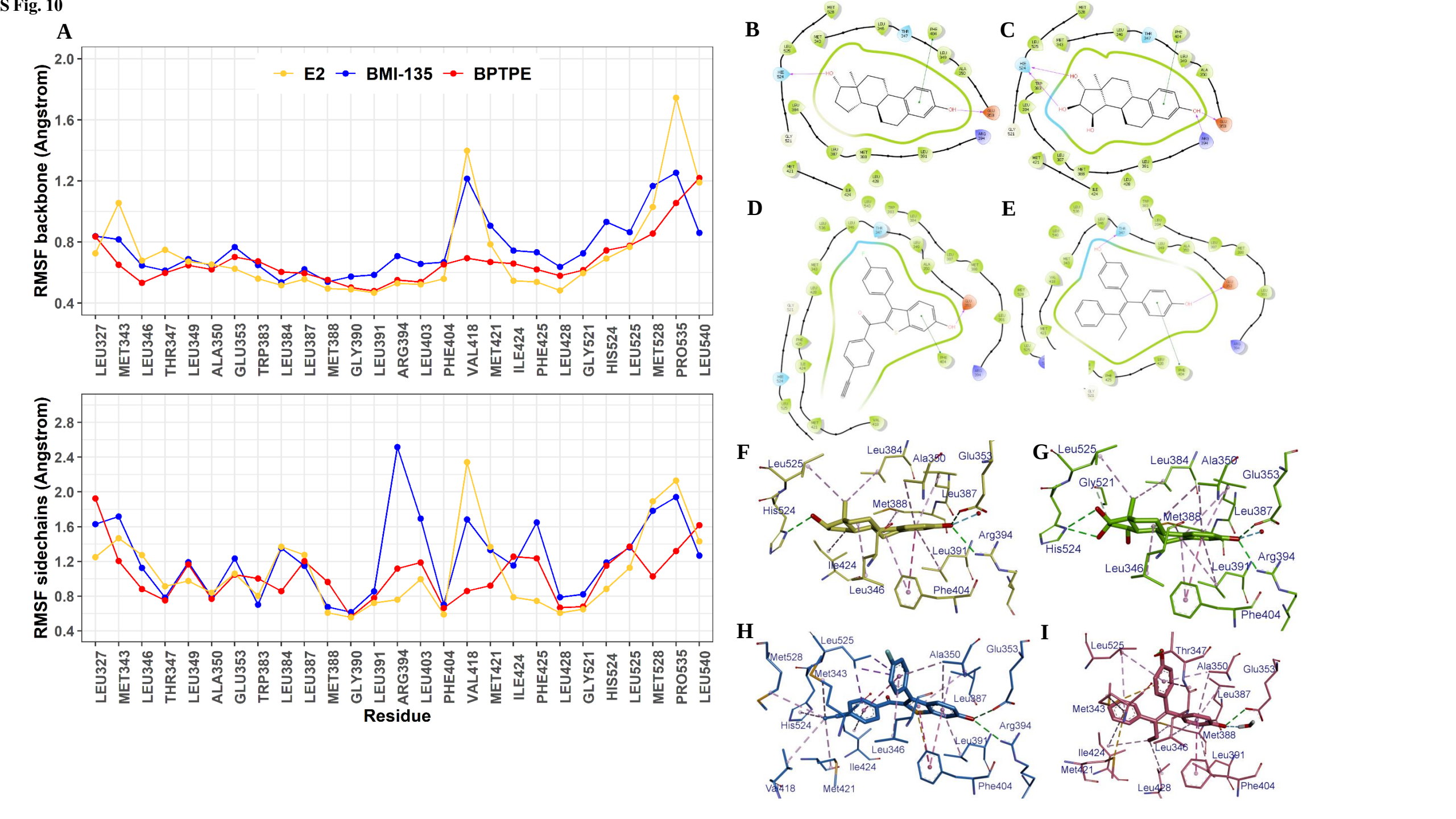
A
E2
BMI-135
BPTPE
RMSF backbone (Angstrom)
RMSF sidechains (Angstrom)
LEU327 MET343 LEU346 THR347 LEU349 ALA350 GLU353 TRP383 LEU384 LEU387 MET388 GLY390 LEU391 ARG394 LEU403 PHE404 VAL418 MET421 ILE424 PHE425 LEU428 GLY521 HIS524 LEU525 MET528 PRO535 LEU540
Residue
B
C
D
E
F
Leu525
Leu384
Ala350
Glu353
Leu387
His524
Met388
Arg394
Leu391
Ile424
Leu346
Phe404
G
Leu525
Gly521
Leu384
Ala350
Glu353
Leu387
Met388
His524
Leu346
Leu391
Arg394
Phe404
H
Leu525
Met528
Met343
Ala350
Glu353
Leu387
His524
Arg394
Leu391
Leu346
Ile424
Val418
Met421
Phe404
I
Leu525
Thr347
Ala350
Glu353
Leu387
Met343
Met388
Leu346
Ile424
Leu391
Met421
Leu428
Phe404

S Fig. 11

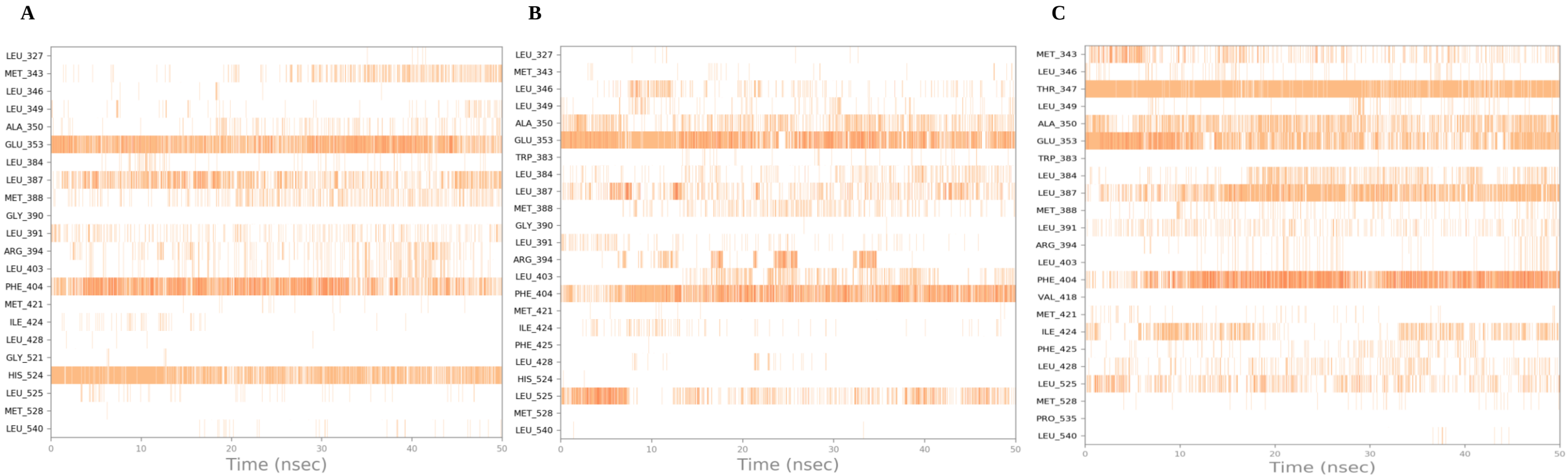
A
B
C
LEU_327
MET_343
LEU_346
LEU_349
ALA_350
GLU_353
LEU_384
LEU_387
MET_388
GLY_390
LEU_391
ARG_394
LEU_403
PHE_404
MET_421
ILE_424
LEU_428
GLY_521
HIS_524
LEU_525
MET_528
LEU_540
TRP_383
PHE_425
THR_347
VAL_418
PRO_535
0
10
20
30
40
50
Time (nsec)